We are IntechOpen,
the world's leading publisher of
Open Access books
Built by scientists, for scientists

6,900
Open access books available

186,000
International authors and editors

200M
Downloads

Our authors are among the

154
Countries delivered to

TOP 1%
most cited scientists

12.2%
Contributors from top 500 universities

BOOK CITATION INDEX
CLARIVATE ANALYTICS
INDEXED

WEB OF SCIENCE™

Selection of our books indexed in the Book Citation Index
in Web of Science™ Core Collection (BKCI)

Interested in publishing with us?
Contact book.department@intechopen.com

Numbers displayed above are based on latest data collected.
For more information visit www.intechopen.com

8

SONAR Images Denoising

Alexandru Isar[1], Ioana Firoiu[2], Corina Nafornita[1] and Sorin Moga[3]
[1]Politehnica University Timisoara,
[2]ALCATEL-LUCENT Timisoara
[3]Institut TELECOM; TELECOM Bretagne, UMR CNRS 3192
Lab-STICC; Université europèenne de Bretagne,
[1,2]Romania
[3]France

1. Introduction

The proliferation of SONAR images produced by different equipments: multibeam echo sounders, side scan sonar, forward looking imaging SONAR…, [Lurton, 2002], and the large number of processing methods, created the necessity of expert systems for assisting the decision making process. An example is the SonarScope, an IFREMER expert system [Ifremer, 2010]. The basic functionality of such an expert system is the representation and the analysis of sonar data, organized as a "multilayer" structure defined by its various attributes (bathymetry, image, angles, and raw data from auxiliary sensors …). These data can be represented and processed using various techniques either classical (signal and/or image processing) or specific to SONAR. The goal of an expert system for SONAR images is to achieve three main tasks: Quality Control, Data Processing and Data Interpretation. There are two classes of signal processing techniques used in an expert system for SONAR images. The first one represents the so-called "image conditioning" methods. The first category of conditioning methods refers to the echoes acquisition, meaning the acquisition of depth, of the across and along-track distance, of the received beam angle, of the numbers of the transmitted and received beam, or of the two-way travel time of the acoustic pulse. The echo acquisition has some features like for example the bottom detection mode. The second category of conditioning method refers to the correction of acquired data. There are techniques to complete the missing data (caused by some acquisition imperfections due to unexpected displacements of the platform where the acoustical transducers are mounted or by the non-uniform movement or deviations from the course of the vessel which tracts the platform) and techniques for the correction of the differences between the directivity characteristics of the sensors. The third type of conditioning techniques consists in data organization and management. SONAR data are arranged as a set of arrows called pings (swath), which correspond to all the soundings acquired in a ping cycle. At the beginning of the ping cycle, each sensor's value is logged: gyro, pitch, roll, positions, etc.

The fourth category of conditioning methods refers to the formation of SONAR images. A SONAR image is thus linked with the sensor's time series, pertaining to that given dataset and in synchronization with each ping. The time series can be plotted as curves, displayed in conjunction with the image. There are few geometric formats used for the SONAR

images: PingBeam, LatLong, PingSamples and PingSwat. The fifth category of conditioning methods refers to the assembling of few neighboring individual images. This could be a technique to produce mosaics or digital terrain models (DTM). Finally the sixth conditioning category of methods refers to the angular correction and despecklisation of SONAR images. The last category of image processing methods represents the aim of this chapter. The second class of signal processing methods applied in SONAR expert systems is represented by the so called intelligent image processing techniques: segmentation, textures analysis, classification,...The aim of this chapter is the despecklisation of SONAR images. The SONAR images are perturbed by speckle. It is of multiplicative nature. The aim of a denoising algorithm is to reduce the noise level, while preserving the image features. The noisy image is:

$$f = s \cdot v \tag{1}$$

where s is the noise-free input image and v the speckle noise. We present the most frequently used despecklisation techniques starting with the classical ones, Lee, Kuan and Frost filters and continuing with the pure statistical despecklisation method proposed in [Walessa&Datcu, 2000] to arrive at the most modern ones which act in the wavelet domain.

2. Denoising methods

The field of natural images denoising methods is very large. A lot of articles dedicated to denoising methods were already written. Most of these articles are focused on the case of additive noise.
There are two ways of reducing the speckle to an additive noise. The first one involves the separation into a sum between the signal and a signal-dependent noise:

$$f = s + s \cdot (v - 1) \tag{2}$$

while the second one simply takes advantage of the properties of the logarithm:

$$\ln f = \ln s + \ln v \tag{3}$$

Assuming that usually f is not stationary, in the first approach the additive noise is not stationary as well, [Argenti et al., 2009]. There are two categories of denoising methods for the additive noise, the methods acting in the spatial domain and the methods which act in a transformed domain. We proceed with the presentation of the first category.

2.1 Denoising based on differential equations with partial derivatives
A first category of images denoising methods acting in the spatial domain are based on differential equations with partial derivatives. These denoising methods do not take into account any a priori information about the image to be processed, being non parametric. The aim of those methods is to consider the denoising like a decomposition of the acquired image into two components, the noiseless part and the noise. This decomposition can be realized by the projection of the acquired image on two very different vector spaces. The projection can be done by the minimization of a cost function. The result corresponds to the solution of the system of equations which is obtained imposing the zero value to the partial

derivatives of the cost function. This is a system of partial differential equations. The simplest projection on the noiseless space is realized averaging the acquired image. The corresponding denoising method works well for the homogeneous regions of the acquired image if the noise is zero mean. Tacking into account the fact that the averager is a low-pass filter, this denoising method distorts the edges and some of the textured regions by oversmoothing.

2.2 Denoising by non-local averaging

Another very modern non parametric denoising method is based on non-local (NL) averaging [Buades, 2007]. The NL-means algorithm tries to take advantage of the high degree of redundancy of any natural image. Every small area (or window) in a natural image has many similar areas in the same image. In a very general sense, one can define as „neighborhood of a pixel i" any set of pixels j in the image so that a window around j looks like a window around i. All pixels in that neighborhood can be used for predicting the value at i. Given a discrete noisy image $x = \{x(i) | i \in I\}$, the estimated value $NL_x(i)$ is computed as a weighted average of all the pixels in the image, $NL_x(i) = \sum_{j \in I} \beta(i, j) x(j)$, where the weights $\{\beta(i, j)\}_j$ depend on the similarity between the pixels i and j and satisfy the usual conditions $0 \le \beta(i, j) \le 1$ and $\sum_j \beta(i, j) = 1$. The non-locality of the average prevents from oversmoothing.

2.3 Denoising using statistical filters

Another category of denoising methods are the parametric ones. These methods take into account statistical models for the noiseless component of the acquired image and for the noise. One of the best parametric denoising methods uses maximum a posteriori (MAP) filters. The MAP estimation of w, based on the observation $y=w+n$, (where n represents the additive noise) is given by the MAP filter equation:

$$\hat{w}(y) = \underset{w}{\operatorname{argmax}} \left\{ \ln \left(p_{\mathbf{n}}(y - w) p_{\mathbf{w}}(w) \right) \right\} \qquad (4)$$

where p_a denotes the probability density function (pdf) of a.

2.3.1 Classical despecklisation filters

Kuan [Kuan et al., 1987] considered a multiplicative speckle model and designed a linear filter based on the minimum mean square error (MMSE) criterion, optimal when both the scene and the detected intensities are Gaussian distributed.

The Lee filter [Lee, 1981] is a particular case of the Kuan filter due to a linear approximation made for the multiplicative noise model.

The Frost filter [Frost et al., 1982] is a Wiener filter adapted to multiplicative noise. The parameters of the Kuan, Lee and Frost filters are: the size of the rectangular windows used for the estimation of the local standard deviation of the useful component of the acquired image and its number of looks.

2.4 Denoising in a transform's domain

Another excellent denoising method for the case of additive noise makes the object of [Katkovnik et al.,2006]. There are a lot of original contributions highlighted in this reference:

the local polynomial analysis of images, the role of anisotropic analysis windows, etc...
Some very clever associations of those notions conduct to very efficient local denoising
methods applied in the spatial domain or in the field of the shape adaptive Digital Cosinus
Transform (SADCT).

2.4.1 Denoising into the wavelets domain

A set of denoising methods for additive noise act in the wavelets domain. These methods
have three steps: the computation of a wavelet transform (WT); the filtering of the detail
wavelet coefficients; the computation of the corresponding inverse WT (IWT). The
usefulness of the filtering in the wavelet domain comes from the sparseness of the WTs.
There are only few wavelet coefficients with high magnitude, which concentrate the most of
the energy of the noiseless component of the input image. The other wavelet coefficients
have small magnitude and can be considered noise. They can be discarded without
producing high distortions.

A first category of denoising methods applied in the wavelets domain is based on non-
parametric techniques [Donoho&Johnstone, 1994] and uses the hard or the soft thresholding
filters. The parent of these methods is Professor David Donoho from Stanford University.
His goal was to estimate the noiseless component of the acquired image by the minimization
of the min-max approximation error. He studied the case of the Discrete Wavelet Transform
(DWT). In the following we will make a general presentation of the wavelet transforms and
we'll continue with the denoising techniques based in these transforms.

2.4.1.1 Wavelet transforms

There are few wavelet transforms (WT) which were used for images denoising. The first one
was the DWT.

2.4.1.1.1 The DWT

All the WTs are characterized by two features: the mother wavelets, MW and the primary
resolution, PR (number of iterations). The importance of their selection is highlighted in
[Nason, 2002]. An appealing particularity of the 2D DWT is the interscale dependency of the
wavelet coefficients. The main advantage of the implementation of the 2D DWT is its
flexibility, as it inherits some of the classes of mother wavelets developed in the framework
of the 1D DWT, like the Daubechies, Symmlet or Coiflet families. The implementation of 1D
DWT is presented in figure 1. It implements an orthonormal multiresolution analysis
[Mallat, 99]. Each of the iterations of the algorithm used for the computation of the 2D DWT
implies several operations. First, the lines of the input image (obtained at the end of the
previous iteration) are passed trough two different filters (a lowpass filter having the
impulse response m_0 and a high-pass filter m_1) resulting two different sub-images. Then the
lines of the two sub-images obtained at the output of the two filters are decimated with a
factor of 2. Next, the columns of the two images obtained are low-pass filtered with m_0 and
high-pass filtered with m_1. The columns of those four sub-images are also decimated with a
factor of 2. Four new sub-images, representing the result of the current iteration (which
corresponds to the current decomposition level (or scale)), are obtained. These sub-images
are called subbands. The first sub-image, obtained after two lowpass filterings, is called
approximation sub-image (or LL subband). The other three are named detail sub-images:
LH, HL and HH. The LL sub-image represents the input for the next iteration. In the
following, the coefficients of the DWT will be denoted with $_xD_m^k$, where x represents the

image who's DWT is computed (considered as a bivariate random signal), *m* represents the current scale and *k* = 1 - for the subband LH, *k* = 2 - for HL, *k* = 3 - for HH and *k* = 4 - for LL. These coefficients are computed using the following relation:

$$_x D_m^k [n_1, p_1] = \left\langle x(\tau_1, \tau_2), \psi_{m,n_1,p_1}^k (\tau_1, \tau_2) \right\rangle,$$

where the wavelets are real functions and can be factorized as:
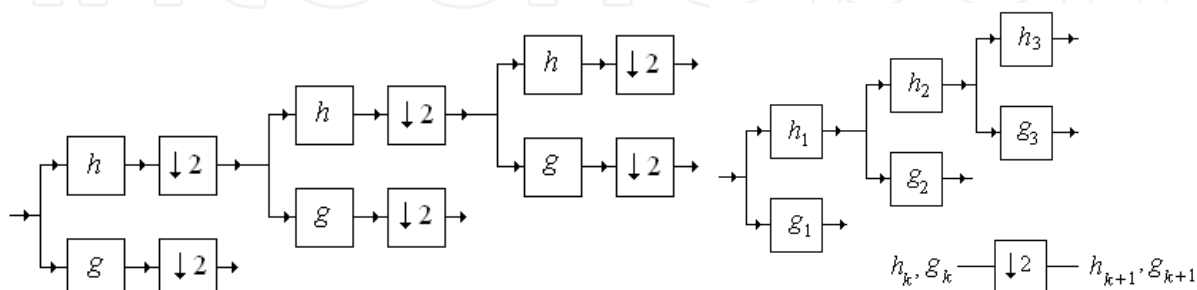
$$\psi_{m,n,p}^k (\tau_1, \tau_2) = \alpha_{m,n}^k (\tau_1) \cdot \beta_{m,p}^k (\tau_2),$$

Fig. 1. (left) 1D DWT implementation. *h* – lowpass filter, *g* - highpass filter. They form a pair of quadrature mirror filters [Mallat, 99]. The filters are followed by decimators with decimation factor equal with 2; (right) UDWT implementation. h_k – lowpass filters, g_k - highpass filters.

and the two factors can be computed using the scale function $\varphi(\tau)$ and the mother wavelets ψ(τ) with the aid of the following relations:

$$\alpha_{m,n}^k (\tau) = \begin{cases} \varphi_{m,n}(\tau), & k = 1, 4 \\ \psi_{m,n}(\tau), & k = 2, 3 \end{cases}, \beta_{m,p}^k (\tau) = \begin{cases} \varphi_{m,p}(\tau), & k = 2, 4 \\ \psi_{m,p}(\tau), & k = 1, 3 \end{cases},$$

where:

$$\varphi_{m,n}(\tau) = 2^{-\frac{m}{2}} \varphi(2^{-m}\tau - n) \text{ and } \psi_{m,n}(\tau) = 2^{-\frac{m}{2}} \psi(2^{-m}\tau - n).$$

Taking into account the last equations it can be written:

$$\psi_{m,n,p}^k (\tau_1, \tau_2) = 2^{-m} \psi^k (2^{-m}\tau_1 - n, 2^{-m}\tau_2 - p) \text{ where } \psi^k (\tau_1, \tau_2) = \psi_{0,0,0}^k (\tau_1, \tau_2).$$

An iteration of the 2D DWT is presented in figure 2. The main disadvantages of the 2D DWT are the poor directional selectivity and the shift sensitivity. Separable filtering along the rows and columns of an image produces four images at each level. The LH and HL bandpass sub-images can select mainly horizontal or vertical edges respectively, but the HH sub-image contains components from diagonal features of either orientation. This means that the separable real 2D DWT has 'poor directional selectivity'. This is illustrated in fig. 3. From left to right we can observe the vertical details (HL), the horizontal details (LH) and the diagonal details (HH). Prof. Kingsbury, in [Kingsbury, 1999] explains this limitation by

the fact that real highpass row filters select both positive and negative horizontal high frequencies and, consequently, the combined HH filter must have pass-bands in all four quadrants of the 2-D frequency plane.
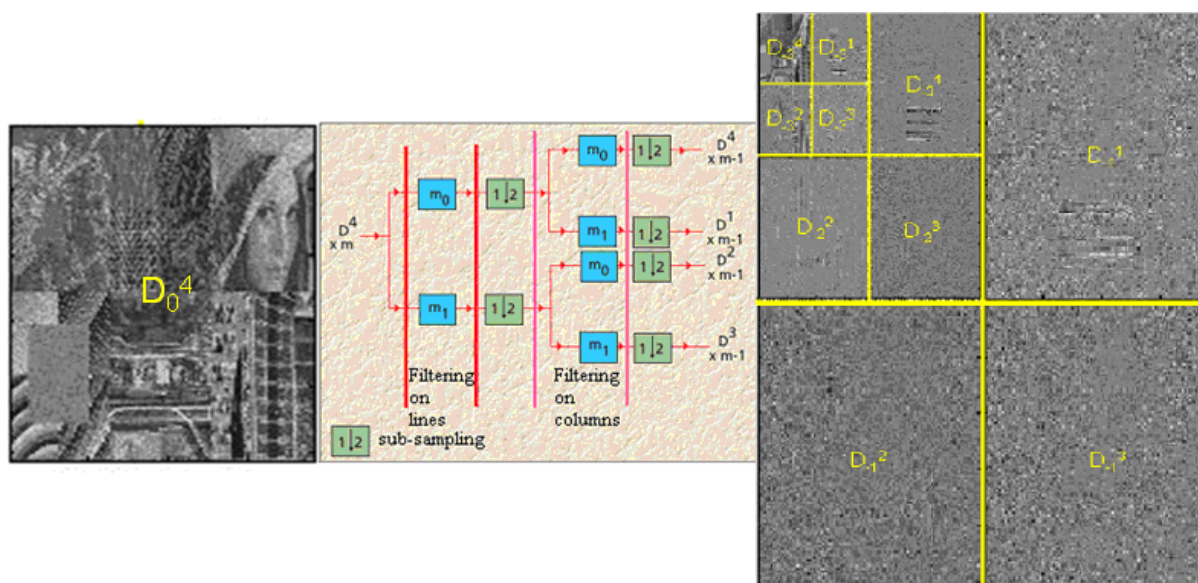

Fig. 2. An iteration of the 2D DWT (middle). The structure of the result obtained applying three iterations of the 2D DWT to the image in the left part of the figure can be seen in the image from the right part of the figure.
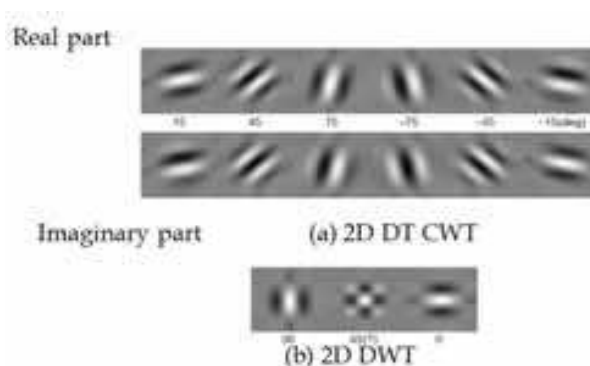

Fig. 3. Basis functions of 2D Q-shift complex wavelets (a) and 2D real wavelet filters (b), all illustrated at level 4 of the transforms. The complex wavelets provide 6 directionally selective filters, while real wavelets provide 3 filters, only two of which have a dominant orientation.

On the other hand, a directionally selective filter for diagonal features with positive gradient must have pass-bands only in quadrants 2 and 4 of the frequency plane, while a filter for diagonals with negative gradient must have pass-bands only in quadrants 1 and 3. The poor directional properties of real separable filters make it difficult to generate steerable or directionally selective algorithms, based on the separable real DWT. Other WTs which overcomes one or both these disadvantages are: the Undecimated Discrete Wavelet Transform (UDWT), the Double Tree Complex Wavelet Transform (DTCWT) and the Hyperanalytic Wavelet Transform (HWT).

2.4.1.1.2 The 2D UDWT

A particular wavelet transform is the undecimated wavelet transform (UWT), also known as the 'Stationary Wavelet Transform' and can be implemented using the 'Algorithme à Trous'. The UDWT refers to the discrete implementation of this transform. The 'Algorithme à Trous', first introduced in [Holschneider et al., 1989] for music synthesis applications, is similar to a non orthonormal multiresolution algorithm for which the discrete wavelet transform is exact. An implementation of the UDWT is presented in figure 1. Due to the absence of decimators in the UDWT's implementation, each coefficient sequence from any level of decomposition has the same length as the original, in other words, if the original signal has N samples, the UDWT L-level representation is of size $N\times(L+1)$, making from the UDWT a highly redundant transform. But eliminating the decimators is obtained a translation invariant WT. The 2D UDWT is shift-invariant (due to the absence of decimators) but it has a poor directional selectivity and is very redundant.

2.4.1.1.3 The 2D DTCWT

In 1998, Kingsbury first introduced the DT CWT [Kingsbury, 1998] that relies on the observation that approximate shift invariance can be achieved with a real DWT by doubling the sampling rate at each level of the tree. For this to work, the samples must be evenly spaced. The sampling rates can be doubled by eliminating the down-sampling by 2 after the level 1 filters. This is equivalent to having two parallel fully-decimated trees a and b, like in fig. 4, provided that the delays of H_{0b} and H_{1b} are one sample offset from H_{0a} and H_{1a}. Kingsbury found that, to get uniform intervals between samples from the two trees below level 1, the filters in one tree must provide delays that are half a sample different (at each filter input rate) from those in the other tree. This statement is also supported by Selesnick who, in [Selesnick, 2001], gives an alternative derivation and explanation of the same result. The implementation of such a transform is done using two mother wavelets, one for each tree, one of them being (approximately) the Hilbert transform of the other. On one hand, the dual-tree DWT can be viewed as an overcomplete wavelet transform with a redundancy factor of two. On the other hand, the dual-tree DWT is also a complex DWT, where the first and second DWTs represent the real and imaginary parts of a single complex DWT. In order to have a visual aspect of the DT CWT, we present in figure 4, the Q-shift version of the DT CWT as it is given in [Kingsbury, 2001]. In order to examine the shift invariance properties of a transform, Kingsbury [Kingsbury, 2001] proposes a method based on the retention of just one type (details or approximations), from just one level of the decomposition tree. For example one might choose to retain only the level-3 detail coefficients and set all the others to zero. If the signal reconstructed from just these coefficients is free of aliasing then it can be said that the transform is shift invariant at that level. The degree of shift invariance of two implementation schemes (one for the DT CWT and the other for the classical DWT) is compared in fig. 5. In each case the input is given by 16 shifted versions of a unitary step signal. Each unitary step is passed through the forward and inverse version of the chosen wavelet transform. The figure shows the input steps and the components of the inverse transform output signal, reconstructed from the wavelet coefficients at each of levels 1 to 4 in turn and from the scaling function coefficients at level 4. Summing these components reconstructs the input steps perfectly. Good shift invariance is shown when all the 16 output components from a given level have the same shape, independent of shift. It is easily observed that the DT CWT has outstanding performances in this direction compared to the severe shift dependence of the normal DWT.

Extension of the DT CWT to two dimensions is achieved by separable filtering along columns and then rows. However, if column and row filters both suppress negative frequencies, then only the first quadrant of the 2-D signal spectrum is retained. It is well known, from 2-D Fourier transform theory, that two adjacent quadrants of the spectrum are required to represent fully a real 2-D signal. Therefore in the DT CWT the image is also filtered with complex conjugates of the row (or column) filters in order to retain a second (or fourth) quadrant of the spectrum. This then gives 4:1 redundancy in the transformed 2-D signal. A schematic representation of the 2D DT CWT based on the even-odd implementation was given by [Jalobeanu et al., 2003]. At level $m = 1$, the 2D DT CWT is simply a non-decimated wavelet transform (using a pair of odd-length filters h^o and g^o) whose coefficients are re-ordered into 4 interleaved images by using their parity. This defines the 4 trees $T = A$, B, C and D. If a and d denotes approximation and detail coefficients ($a^0 = x$, the input image), we have:

Tree T	A	B	C	D
$\left(a_T^1\right)_{x,y}$	$\left(a^0 * h^o h^o\right)_{2x,2y}$	$\left(a^0 * h^o h^o\right)_{2x,2y+1}$	$\left(a^0 * h^o h^o\right)_{2x+1,2y}$	$\left(a^0 * h^o h^o\right)_{2x+1,2y+1}$
$\left(d_T^{1,1}\right)_{x,y}$	$\left(a^0 * g^o h^o\right)_{2x,2y}$	$\left(a^0 * g^o h^o\right)_{2x,2y+1}$	$\left(a^0 * g^o h^o\right)_{2x+1,2y}$	$\left(a^0 * g^o h^o\right)_{2x+1,2y+1}$
$\left(d_T^{1,2}\right)_{x,y}$	$\left(a^0 * h^o g^o\right)_{2x,2y}$	$\left(a^0 * h^o g^o\right)_{2x,2y+1}$	$\left(a^0 * h^o g^o\right)_{2x+1,2y}$	$\left(a^o * h^o g^o\right)_{2x+1,2y+1}$
$\left(d_T^{1,3}\right)_{x,y}$	$\left(a^0 * g^o g^o\right)_{2x,2y}$	$\left(a^0 * g^o g^o\right)_{2x,2y+1}$	$\left(a^0 * g^o g^o\right)_{2x+1,2y}$	$\left(a^0 * g^o g^o\right)_{2x+1,2y+1}$

For all other scales ($j > 1$), the transform involves an additional pair of filters, even-length, denoted h^e and g^e. There must be a half-sample shift between the trees to achieve the approximate shift invariance. Therefore, different length filters are used for each tree, i.e. it is necessary to combine h^e, g^e with h^o, g^o, the 4 possible combinations corresponding to the 4 trees:

Tree T	A	B	C	D
$\left(a_T^{j+1}\right)_{x,y}$	$\left(a_A^j * h^e h^e\right)_{2x,2y}$	$\left(a_B^j * h^e h^o\right)_{2x,2y+1}$	$\left(a_C^j * h^o h^e\right)_{2x+1,2y}$	$\left(a_D^j * h^o h^o\right)_{2x+1,2y+1}$
$\left(d_T^{j+1,1}\right)_{x,y}$	$\left(a_A^j * g^e h^e\right)_{2x,2y}$	$\left(a_B^j * g^e h^o\right)_{2x,2y+1}$	$\left(a_C^j * g^o h^e\right)_{2x+1,2y}$	$\left(a_D^j * g^o h^o\right)_{2x+1,2y+1}$
$\left(d_T^{j+1,2}\right)_{x,y}$	$\left(a_A^j * h^e g^e\right)_{2x,2y}$	$\left(a_B^j * h^e g^o\right)_{2x,2y+1}$	$\left(a_C^j * h^o g^e\right)_{2x+1,2y}$	$\left(a_D^j * h^o g^o\right)_{2x+1,2y+1}$
$\left(d_T^{j+1,3}\right)_{x,y}$	$\left(a_A^j * g^e g^e\right)_{2x,2y}$	$\left(a_B^j * g^e g^o\right)_{2x,2y+1}$	$\left(a_C^j * g^o g^e\right)_{2x+1,2y}$	$\left(a_D^j * g^o g^o\right)_{2x+1,2y+1}$

The trees are processed separately, as in a real transform. The combination of odd and even filters depends on each tree. The transform is achieved by a fast Filter Bank (FB) technique, of complexity $O(N)$. The reconstruction is done in each tree independently, by using the dual filters. To obtain a^0, the results of the 4 trees are averaged. This ensures the symmetry between them, thus enabling the desired shift invariance. The complex coefficients are obtained by combining the different trees together. If the subbands are indexed by k, the detail subbands $d^{j,k}$ of the parallel trees A, B, C and D are combined to form complex subbands $z_+^{j,k}$ and $z_-^{j,k}$, by the linear transform:

$$z_+^{j,k} = \left(d_A^{j,k} - d_D^{j,k}\right) + i\left(d_B^{j,k} + d_C^{j,k}\right) \quad z_-^{j,k} = \left(d_A^{j,k} + d_D^{j,k}\right) + i\left(d_B^{j,k} - d_C^{j,k}\right) \tag{5}$$

Complex filters in multiple dimensions can provide true directional selectivity, despite being implemented separately, because they are still able to separate all parts of the m-D frequency space. For example the 2D DT CWT produces six bandpass sub-images of complex coefficients at each level, which are strongly oriented at angles ±15º, ±45º, ±75º, as illustrated by the level 4 impulse responses in fig. 3.
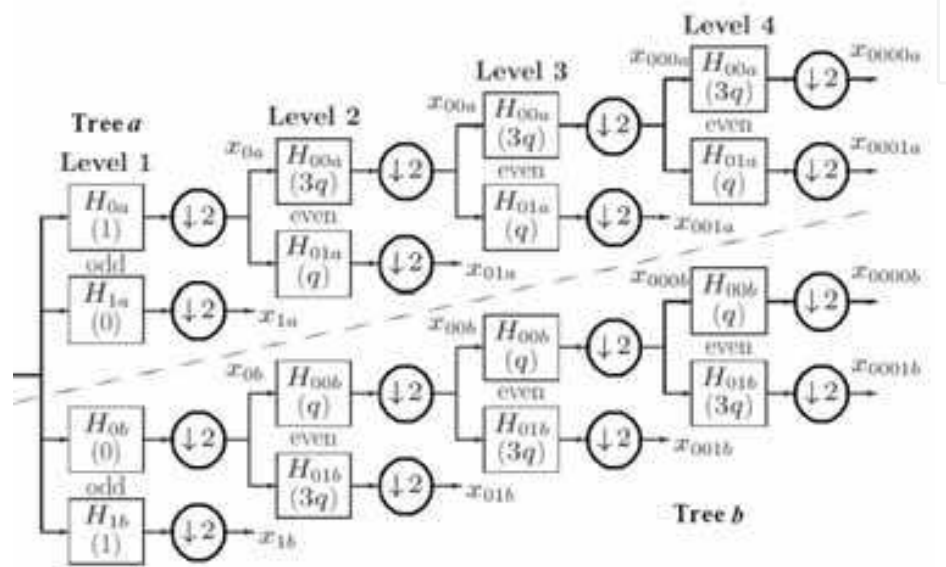
Fig. 4. The Q-shift version of the DT CWT as it is given in [Kingsbury, 2001].
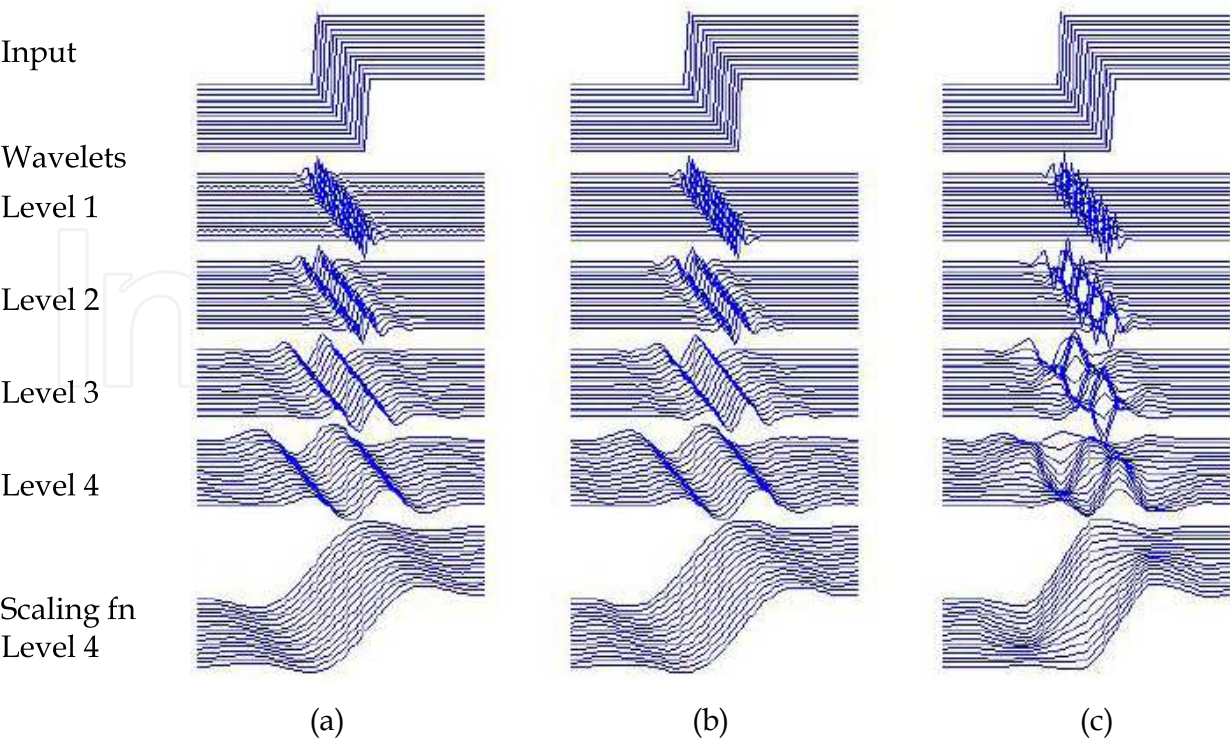
Fig. 5. A comparison of the shift invariance of three WTs: ADWT (a), DTCWT (b) and DWT (c).

Components of reconstructed 'disc' image

HWT

2D DT CWT

2D DWT

wavelets: level 1   level 2   level 3   level 4 Scaling fn. level 4
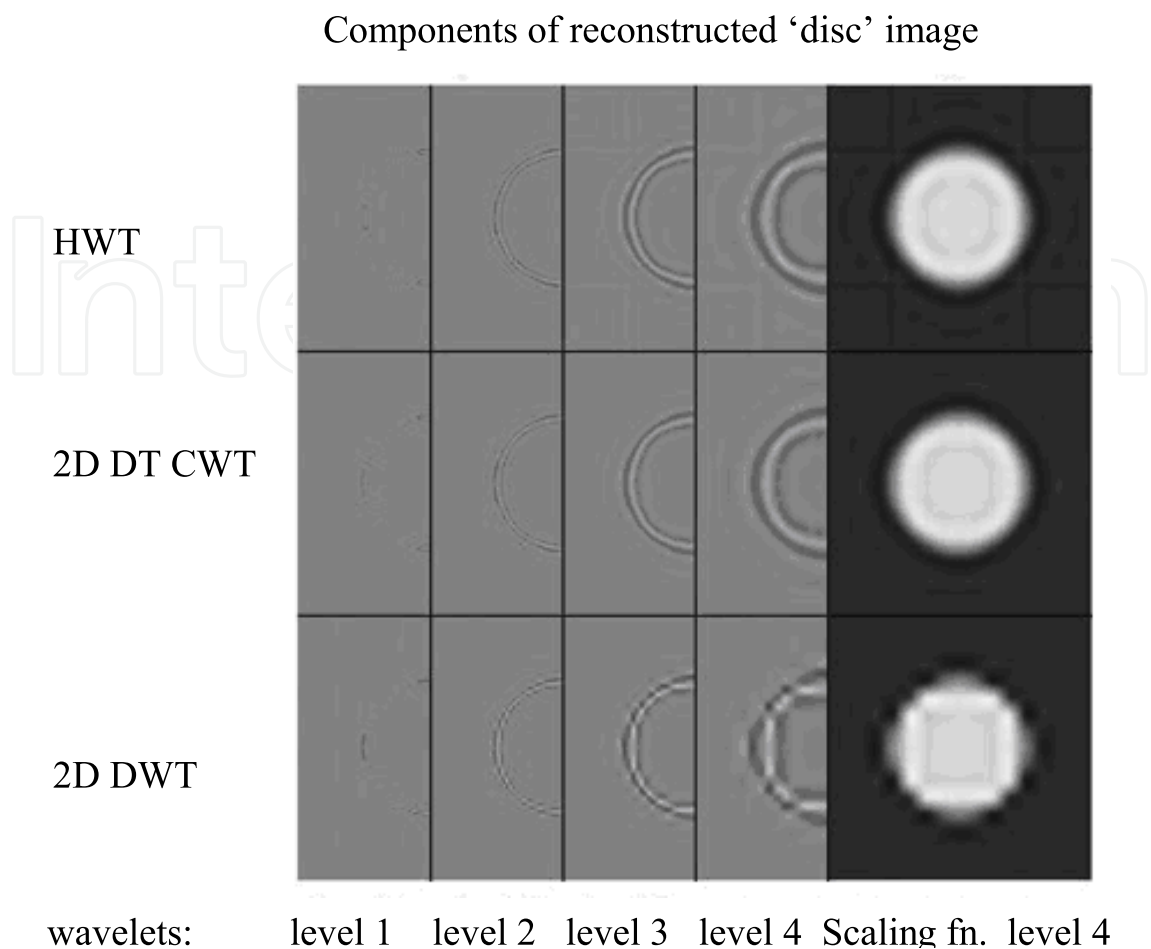
Fig. 6. Wavelet and scaling function components at levels 1 to 4 of an image of a light circular disc on a dark background, using the HWT (upper row), the 2D DT CWT (middle row) and 2D DWT (lower row). Only half of each wavelet image is shown.

In order to obtain these directional responses, it is necessary to interpret the scaling function (lowpass) coefficients from the two trees as complex pairs (rather than as purely real coefficients at double rate) so that they can be correctly combined with wavelet (highpass) coefficients, which are also complex, to obtain the filters oriented at $\pm 15^{\circ}$ and $\pm 75^{\circ}$ (see 5). The main property of the 2D DT CWT is the quasi shift invariance, as shown by Kingsbury in [Kingsbury, 2001] i.e. the magnitudes $|z_{\pm}|$ are nearly invariant to shifts of the input image. The shift invariance is perfect at level 1, and approximately achieved beyond this level: the transform algorithm is designed to optimize this property. In fig. 6, the shift-dependence properties of the 2D DT CWT were compared with the 2D DWT. The input is now an image of a light circular disc on a dark background. This circular form is suited for the analysis of the shift dependence in 2D as neighbor pixels from the contour of the disc can be interpreted as obtained through 2D shifts. The rows of images, from left to right in fig. 6, show the components of the output image, reconstructed from the 2D DT CWT wavelet coefficients at levels 1, 2, 3 and 4 and from the scaling function coefficients at level 4. The lower row of images show the equivalent components when the fully decimated 2D DWT is used instead. In the lower row, we see substantial aliasing artifacts, manifested as

irregular edges and stripes that are almost normal to the edge of the disc in places. Contrast this with the row of 2D DT CWT images, in which artifacts are virtually absent. The smooth and continuous images here demonstrate good shift invariance because all parts of the disc edge are treated equivalently; there is no shift dependence.

2.4.1.1.4 The HWT

In [Abry, 1994] is demonstrated that approximate shiftability is possible for the DWT with a small, fixed amount of transform redundancy. In this reference is designed a pair of real mother wavelets such that one is approximately the Hilbert transform of the other. This wavelet pair defines an analytic discrete wavelet transform (ADWT) presented in figure 7 a). A complex wavelet coefficient is obtained by interpreting the wavelet coefficient from one DWT tree as being its real part, whereas the corresponding coefficient from the other tree is interpreted as its imaginary part. The implementation of the ADWT is presented in figure 7 b). We first apply a Hilbert transform to the data. The real wavelet transform is then applied to the analytical signal associated to the input data, obtaining complex coefficients. The two implementations of the ADWT presented in figure 7 are equivalent because:

$$d_{ADWT}[m,n] = \langle x(t), \psi_{m,n}(t) + i\mathrm{H}\{\psi_{m,n}(t)\}\rangle = \langle x(t), \psi_{m,n}(t)\rangle - i\langle x(t), \mathrm{H}\{\psi_{m,n}(t)\}\rangle =$$
$$= \langle x(t), \psi_{m,n}(t)\rangle + i\langle \mathrm{H}\{x(t)\}, \psi_{m,n}(t)\rangle = \langle x(t) + i\mathrm{H}\{x(t)\}, \psi_{m,n}(t)\rangle \tag{6}$$
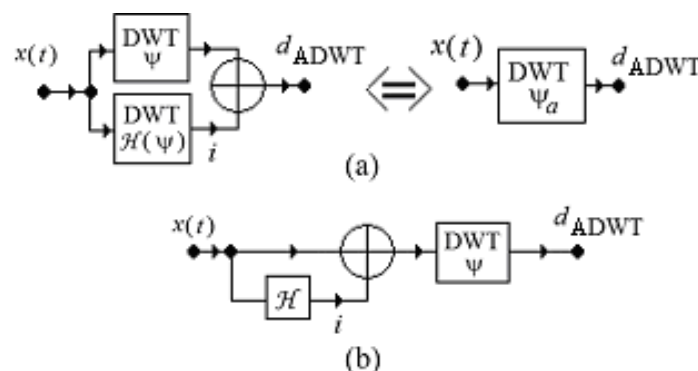

Fig. 7. Three equivalent implementations of the ADWT. (a) The double tree of real DWTs is equivalent with a complex DWT, which can be reduced at the input (b).

In fact neither the DTCWT nor the proposed implementation of ADWT correspond to perfect analytic mother wavelets, because the exact digital implementation of a Hilbert transform pair of mother wavelets with good performance is not possible in the case of the first transform (due to the fractional delay between the two trees required) and because the digital Hilbert transformer is not a realizable system in the case of the second transform. The DTCWT requires special mother wavelets (the implementation of the ADWT proposed in figure 7 b) can be realized using classical mother wavelets like those conceived by Daubechies) but can assure a higher degree of shift invariance. These two transforms have in the 1D case a redundancy of 2. In order to evaluate the shift-invariance performance of ADWT we make a visual evaluation of the degree of shift invariance by taking the same test professor Kingsbury has proposed in [Kingsbury, 2001]. We have used this test to make a comparison between ADWT, DT CWT, and the classical DWT. As can be seen, we obtain, using Daubechies 10-taps filter, results comparable with those obtained by Kingsbury. From

fig. 5 it can be observed that the DWT is not shift-invariant; the lines of coefficients corresponding to different shifts are not parallel, while the ADWT and DT CWT are quasi shift-invariant.

All the 1D WTs already mentioned have simpler or more complicated 2D generalizations. The generalization of the analyticity concept in 2D is not obvious, because there are multiple definitions of the Hilbert transform in this case. In the following we will use the definition of the analytic signal associated to a 2D real signal named hypercomplex signal. So, the hypercomplex mother wavelets associated to the real mother wavelets $\psi(x,y)$ is defined as:

$$\psi_a(x,y) = \psi(x,y) + i H_x\{\psi(x,y)\} + j H_y\{\psi(x,y)\} + k H_x\{H_y\{\psi(x,y)\}\} \tag{7}$$

where $i^2 = j^2 = -k^2 = -1$, and $ij = ji = k$, [Davenport, 2010]. The HWT of the image $f(x,y)$ is: $HWT\{f(x,y)\} = \langle f(x,y), \psi_a(x,y)\rangle$. Tacking into account relation (7) it can be written:

$$
\begin{aligned}
HWT\{f(x,y)\} &= DWT\{f(x,y)\} + iDWT\{H_x\{f(x,y)\}\} + \\
&+ jDWT\{H_y\{f(x,y)\}\} + kDWT\{H_y\{H_x\{f(x,y)\}\}\} = \\
&\langle f_a(x,y), \psi(x,y)\rangle = DWT\{f_a(x,y)\}.
\end{aligned}
\tag{8}
$$

So, the HWT of the image $f(x,y)$ can be computed with the aid of the 2D DWT of its associated hyper complex image. Consequently, the HWT of the image $f(x,y)$ can be computed with the aid of the 2D DWT of its associated hyper complex image. The HWT implementation uses four trees, each one implementing a 2D DWT. The first tree is applied to the input image. The second and the third trees are applied to 1D Hilbert transforms computed across the lines (H_x) or columns (H_y) of the input image. The fourth tree is applied to the result obtained after the computation of the two 1D Hilbert transforms of the input image.

The enhancement of the directional selectivity of the HWT is realized like in the case of the 2D DTCWT, by the separation of the real and imaginary parts of the complex coefficients belonging to each subband of the WT (eq. 5). The HWT implementation is presented in figure 8.
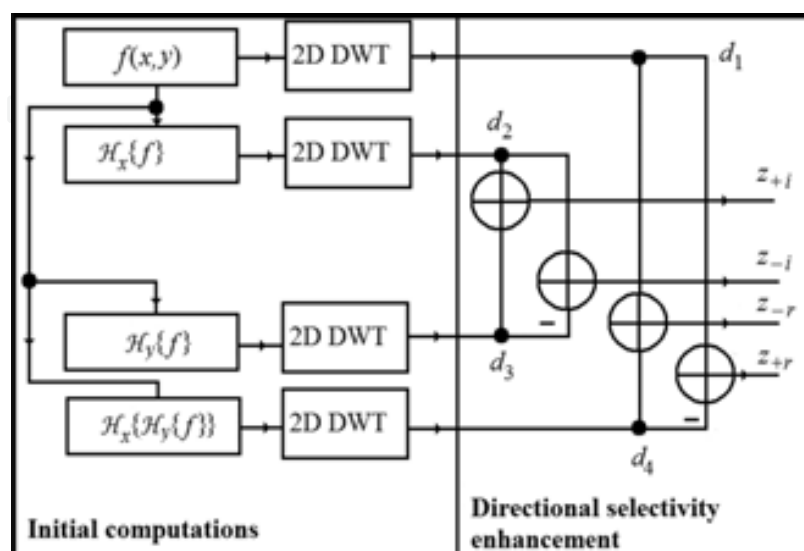

Fig. 8. HWT implementation architecture.

Let us consider, for example, the case of the diagonal detail subbands, (HH), presented in figure 9. We selected a particular input image, $f(x,y) = \delta(x,y)$, to appreciate the frequency responses associated to different transfer functions represented in figure 8. More precisely, the example in figure 9 refers to the transfer functions that relate the input f with the outputs z_{-r} and z_{+r}. The spectrum of the input image $F\{\delta(x,y)\}(f_x,f_y)$ is constant. For the subband HH of each 2D DWT we have two preferential orientations, corresponding to the two diagonals ($\pm\pi/4$). So, the 2D DWT cannot separate these two orientations. But the spectra of the coefficients obtained after linear combinations, for example z_{-r} and z_{+r}, $F\{^{HH}z_{-r}\}(f_x,f_y)$ and $F\{^{HH}z_{+r}\}(f_x,f_y)$, have only one preferential direction, the second diagonal respectively the first one.
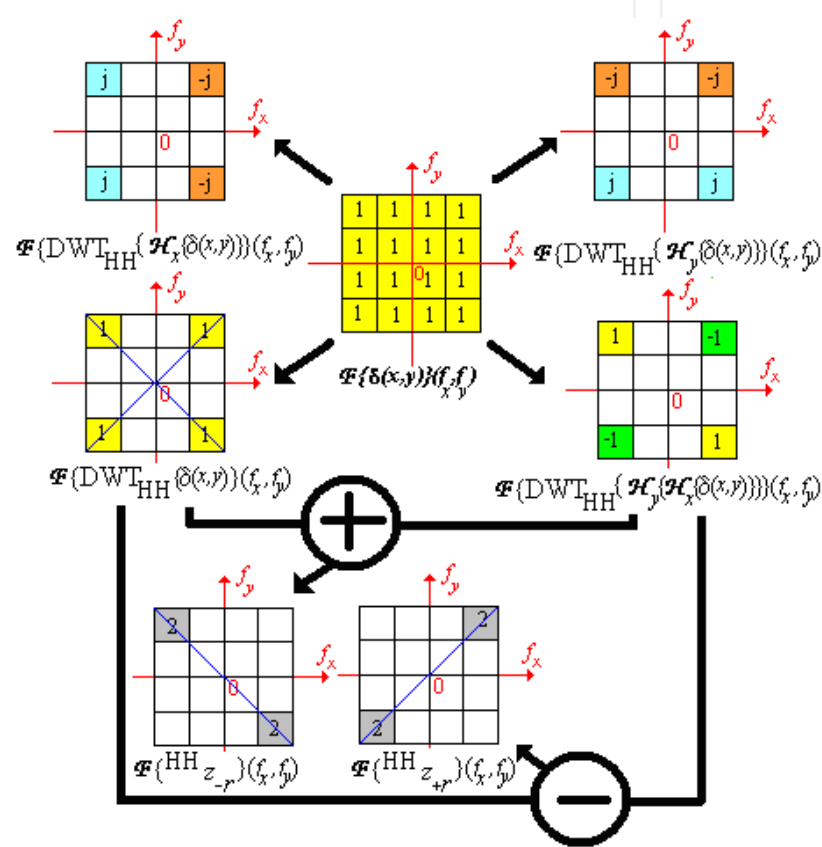
Fig. 9. The strategy of directional selectivity enhancement in the HH subband. The frequency responses of the systems that transform the input image *f* into the output diagonal detail coefficient sub-images *z_-r* and *z+r* represented in figure 12.

In conclusion, by using the HWT these directions can be separated. The same strategy can be used to enhance the directional selectivity in the other two subbands: LH and HL, obtaining the preferential orientations: $\pm\mathrm{atan}(2)$ and $\pm\mathrm{atan}(1/2)$. A comparison of the directional selectivity of the 2D DWT and HWT, implemented as proposed in figure 8, is presented in figure 10. We have conceived a special input image, in the frequency domain, to conduct this simulation. Its spectrum, represented in figure 10, is oriented following the directions: 0, $\pm\mathrm{atan}(1/2)$, $\pm\pi/4$, $\pm\mathrm{atan}(2)$ and π. Like the 2D DTCWT, the HWT implemented as proposed in figure 8, has six preferential orientations: $\pm\mathrm{atan}(1/2)$, $\pm\pi/4$ and $\pm\mathrm{atan}(2)$. The 2D-DWT has only three preferential orientations: 0, $\pi/4$ and $\pi/2$, it does not

make the difference between the two principal diagonals. The better directional selectivity of the proposed implementation of HWT versus the 2D DWT can be easily observed, comparing the corresponding detail sub-images in figure 10. For the diagonal detail sub-images, for example, the imaginary part of the HWT rejects the directions: -atan(1/2), $-\pi/4$ and -atan(2), whereas the 2D DWT conserves these directions. Concerning the 2D shift invariance, in figure 6 is presented a comparison between the HWT and the 2D DTCWT.
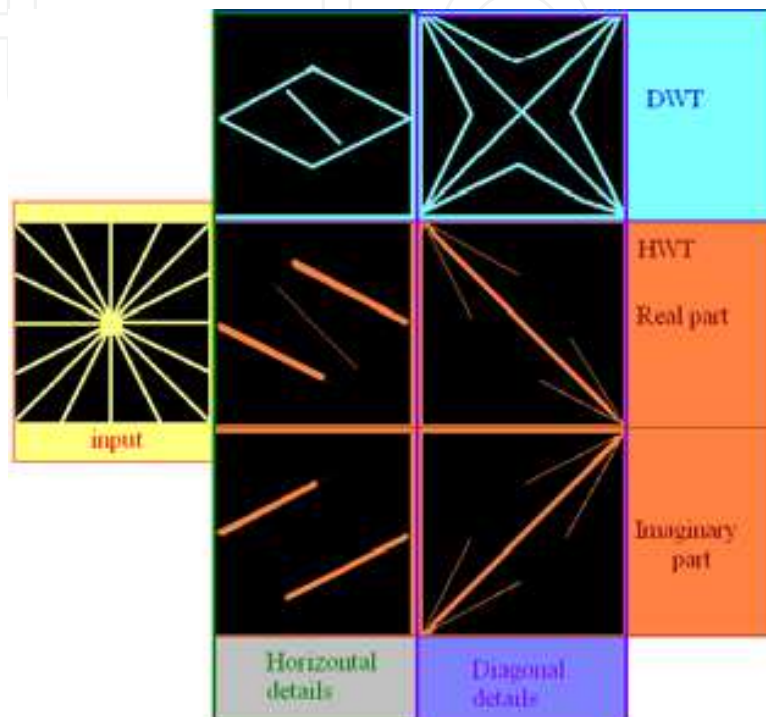
Fig. 10. The absolute values of the spectra of horizontal and diagonal detail sub-images obtained after the first iterations of 2D DWT and HWT (proposed implementation). In the HWT case, the real and imaginary parts of complex coefficients are separated.

The two complex WTs outperform the 2D DWT. The behavior of the HWT is quite similar with the comportment of the 2D DTCWT. One of the goals of the present chapter is to compare the efficiency of those WTs in despecklisation. A second goal of this chapter is to compare the efficiency of the filters applied in the wavelet domain for SONAR despecklisation.

2.4.1.2 MAP Filters in the wavelets domain

As was already said, after the transformation of the multiplicative noise into an additive one based on equations (2) or (3), the WT of the signal obtained is computed. Tacking into account the linearity of the WT, it can be written the equation $y=w+n$, where the first term in the right hand member represents the WT of the noiseless component and the second term represents the WT of the noise. Then the MAP filter equation (4) must be solved. Its solution depends on the selection of the models of pdfs for the noiseless component and for the noise. There are two categories of MAP filters: marginal (both pdfs are univariate functions) and joint (both pdfs are multi-variate functions).

The simpler MAP filter is the marginal zero order Wiener filter. It is constructed considering that the noiseless component of the acquired image and the noise are Gaussian distributed.

2.4.1.2.1 The zero order Wiener filter

We will derive first the joint zero order Wiener filter considering that both pdfs are d-dimensional zero mean Gaussians:

$$p_{\mathbf{w}}(\mathbf{w}) = \frac{1}{(2\pi)^{\frac{d}{2}}|\mathbf{C_w}|^{\frac{1}{2}}} \cdot e^{-\frac{\mathbf{w}^T \cdot \mathbf{C_w^{-1}} \cdot \mathbf{w}}{2}} \text{ and } p_{\mathbf{n}}(\mathbf{n}) = \frac{1}{(2\pi)^{\frac{d}{2}}|\mathbf{C_n}|^{\frac{1}{2}}} \cdot e^{-\frac{\mathbf{n}^T \cdot \mathbf{C_n^{-1}} \cdot \mathbf{n}}{2}} \tag{9}$$

where the covariance matrix of vector $\mathbf{a}$ was denoted by $\mathbf{C_a}$ and its determinant by $|\mathbf{C_a}|$, for d=1. Then, the MAP filter equation (4) becomes:

$$\hat{\mathbf{w}}(\mathbf{y}) = \underset{\mathbf{w}}{\operatorname{argmax}} \left\{ \ln \left(\frac{1}{(2\pi)^d \cdot |\mathbf{C_w}|^{\frac{1}{2}} \cdot |\mathbf{C_n}|^{\frac{1}{2}}} \cdot e^{-\frac{(\mathbf{y}-\mathbf{w})^T \cdot \mathbf{C_n^{-1}} \cdot (\mathbf{y}-\mathbf{w})}{2}} \cdot e^{-\frac{(\mathbf{w})^T \cdot \mathbf{C_w^{-1}} \cdot (\mathbf{w})}{2}} \right) \right\} \tag{10}$$

or:

$$\hat{\mathbf{w}}(\mathbf{y}) = \underset{\mathbf{w}}{\operatorname{argmax}} \left\{ \ln \frac{1}{(2\pi)^d \cdot |\mathbf{C_w}|^{\frac{1}{2}} \cdot |\mathbf{C_n}|^{\frac{1}{2}}} - \frac{(\mathbf{y} \cdot \mathbf{w})^T \cdot \mathbf{C_n^{-1}} \cdot (\mathbf{y} \cdot \mathbf{w})}{2} - \frac{\mathbf{w}^T \cdot \mathbf{C_w} \cdot \mathbf{w}}{2} \right\}$$

problem which is equivalent with the equation obtained by putting the derivative of the argument of the right hand side member equal with zero:

$$\frac{\partial}{\partial \mathbf{w}} \left\{ (\mathbf{y}-\mathbf{w})^T \cdot \mathbf{C_n^{-1}} \cdot (\mathbf{y}-\mathbf{w}) + (\mathbf{w})^T \cdot \mathbf{C_w^{-1}} \cdot (\mathbf{w}) \right\} = 0 \tag{11}$$

Considering the following forms of the d-dimensional vectors:

$$\mathbf{y} = [y_1, y_2, ..., y_d] \; ; \; \mathbf{w} = [w_1, w_2, ..., w_d]$$

where the elements are zero mean independent random variables a_k, k=1,2,…,d, with variances ${}_a\sigma_k^2$, the expression of the covariance matrix becomes:

$$\mathbf{C_a} = \prod_{k=1}^{d} {}_a\sigma_k^2 \cdot \mathbf{I}$$

where $\mathbf{I}$ represents the $d \times d$ unitary matrix. Its determinant is expressed by:

$$|\mathbf{C_a}| = \prod_{k=1}^{d} {}_a\sigma_k^2 = {}_aP$$

So, the multi-variate pdf of the Gaussian random process from (9), for independent univariate components can be put in the equivalent form:

$$p_{\mathbf{a}}(\mathbf{a}) = \frac{1}{(2\pi)^{\frac{d}{2}}|\mathbf{C_a}|^{\frac{1}{2}}} \cdot e^{-\frac{\mathbf{a}^{\mathrm{T}} \cdot \mathbf{C_a^{-1}} \cdot \mathbf{a}}{2}} = \frac{1}{(2\pi)^{\frac{d}{2}}{}_aP^{\frac{1}{2}}} \cdot e^{-\frac{\sum\limits_{k=1}^{d}\frac{a_k^2}{a\sigma_k^2}}{2}} \tag{12}$$

If all the independent random variables a_k, k=1,2,...,d , have the same variances ${}_a\sigma^2$, then the last equations became:

$$\mathbf{C_a} = ({}_a\sigma)^{2d} \cdot \mathbf{I}, \; |\mathbf{C_a}| = {}_a^iP = ({}_a\sigma)^{2d}, \; \mathbf{C_a^{-1}} = ({}_a\sigma)^{-2} \cdot \mathbf{I},$$

$$p_{\mathbf{a}}(\mathbf{a}) = \frac{1}{(2\pi)^{\frac{d}{2}}({}_a\sigma)^d} \cdot e^{-\frac{\|\mathbf{a}\|^2}{2({}_a\sigma)^2}}. \tag{13}$$

Substituting (13) into equation (11), the following system of equations is obtained.

$$\frac{\partial}{\partial w_k}\left\{\sum_{k=1}^{d}\frac{(y_k - w_k)^2}{{}_n\sigma_k^2} + \sum_{k=1}^{d}\frac{w_k^2}{{}_w\sigma_k^2}\right\} = 0, \, k = 1, 2, ..., d \; \Leftrightarrow \; \frac{2}{{}_n\sigma_k^2}(w_k - y_k) + \frac{2}{{}_w\sigma_k^2}w_k = 0 \; \Leftrightarrow$$

$$\Leftrightarrow \; \hat{w}_k = \frac{\dfrac{1}{{}_n\sigma_k^2}}{\dfrac{1}{{}_n\sigma_k^2} + \dfrac{1}{{}_w\sigma_k^2}}y_k \; \Leftrightarrow \; \hat{w}_k = \frac{{}_w\sigma_k^2}{{}_w\sigma_k^2 + {}_n\sigma_k^2}y_k.$$

The solution can be also written in matrix form:

$$\hat{\mathbf{w}} = \mathbf{C_w} \cdot (\mathbf{C_w} + \mathbf{C_n})^{-1} \cdot \mathbf{y} \tag{14}$$

This is the expression of the **joint zero order Wiener estimator.** For d=1, the last equation can be written in the particular form:

$$_wP = {}_w\sigma_1^2 = \sigma^2, \; {}_nP = {}_n\sigma_1^2 = \sigma_n^2, \; \hat{w}_1 = \frac{\sigma^2}{\sigma^2 + \sigma_n^2}y_1 \; \text{or} \; \hat{w} = \frac{\sigma^2}{\sigma^2 + \sigma_n^2}y \tag{15}$$

This is the input-output relation of the marginal zero order Wiener filter. Unfortunately, the two variances in the last equation are not known a priori. The noise variance can be estimated globally, using the diagonal detail sub image obtained at the first decomposition level, D_1^3 (denoted by HH) of a 2D DWT applied to the acquired image, using the following equation:

$$\hat{\sigma}_n^2 = \left[\frac{\text{median}(|y_i|)}{0.6745}\right]^2 , \; y_i \in \text{subband HH} \tag{16}$$

Generally, the variance σ^2 changes in space. This is the reason why is preferable to estimate locally this quantity. Practically the Wiener filtering is realized pixel wise (for each pixel of coordinates (α, β)). For this purpose is used a window, for example of rectangular form,

centered on the pixel of coordinates (α, β) and of size $(2P+1) \times (2P+1)$ denoted by $F_P(\alpha, \beta)$, and the variance is locally estimated inside the window. First is estimated the local expectation of the acquired image:

$$\hat{{}_l\mu}[\alpha,\beta] = \frac{1}{(2P+1)^2} \sum_{(k,l)\in F_P(\alpha,\beta)} y[k,l] \tag{17}$$

and next its local variance :

$$\hat{{}_l\sigma}{}^2{}_y[\alpha,\beta] = \frac{1}{(2P+1)^2} \sum_{(k,l)\in F_P(\alpha,\beta)} \left(y[k,l] - \hat{{}_l\mu}[\alpha,\beta] \right)^2 \tag{18}$$

Using these values, the local variance of the noiseless component is computed by:

$$\hat{{}_l\sigma}{}^2[\alpha,\beta] = \max\left(0, \hat{{}_l\sigma}{}^2{}_y[\alpha,\beta] - \hat{\sigma}_n^2 \right) \tag{19}$$

The zero order Wiener filter can be applied in association with the 2D DWT or 2D DT CWT or HWT. Its main disadvantage is the fact that the model considered for the noiseless image is not adequate because the wavelet coefficients have a heavy tail distribution (due to the sparseness of the WTs). Due to the sparseness of the WTs of the noiseless component, its distribution is heavy tailed. Indeed, there are only few wavelet coefficients with high magnitude; the majority of the wavelet coefficients have small magnitudes producing the heavy tails of the distribution. This affirmation is verified with the aid of the following experiment.

The histograms of different subbands obtained applying the HWT to the image Lena are computed. The results are represented in figure 11. The linear dependencies of the two branches of the logarithms of the histograms prove that the pdfs of the real and imaginary parts of the HWT coefficients correspond to exponential laws (which are heavy tailed):

$$\log\left(K_1 \cdot e^{-|x|} \right) = K_2 - |x| \tag{20}$$

where K_1 and K_2 represent two constants. The Gaussian model supposed for the construction of the marginal zero order Wiener filter does not correspond to the linear dependencies of the two branches of the histograms:

$$\log\left(K_1 \cdot e^{-K_2 x^2} \right) = K_3 - K_2 x^2 \neq K_3 - |x| \tag{21}$$

So, the hypothesis that the real and imaginary parts of the useful HWT coefficients are distributed following Laplace (exponential) laws can be made.

Taking into consideration the histograms of the noiseless wavelet coefficients it can be observed that their repartition is heavy-tailed. The majority of the wavelet coefficients have small magnitude (close to zero). So, the repartition of the wavelet coefficients can be considered of Laplace type.

On the basis of this hypothesis, another MAP filter named adaptive soft thresholding can be constructed.

Re{z_-} - diagonal details, first iteration

Re{ z_-} – horizontal details, first iteration

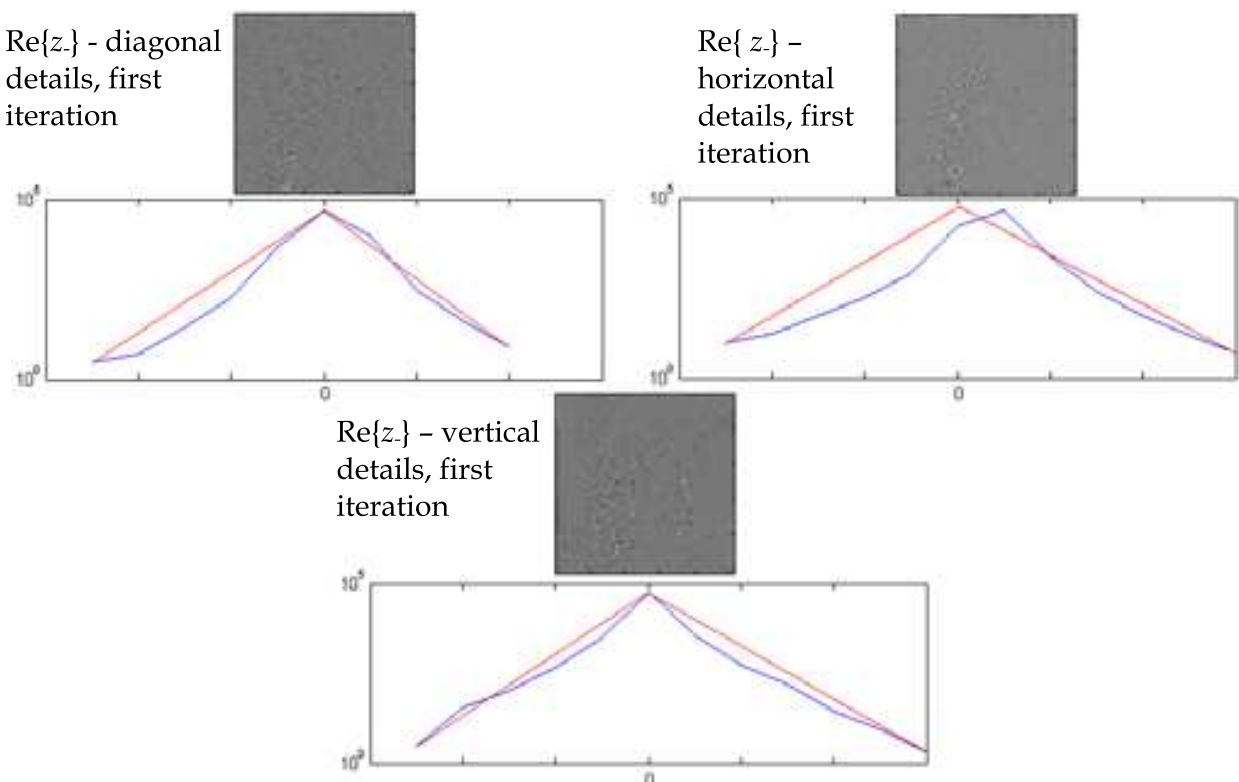

Re{z_-} – vertical details, first iteration

Fig. 11. The histograms of some subbands of the HWT of the image Lena computed using the mother wavelets Dau_20 are represented semi logarithmically (on the vertical axis are represented the logarithms of the values of the histograms) in blue. The corresponding linear dependencies are represented in red.

2.4.1.2.2 The adaptive soft-thresholding filter

If n is Gaussian distributed and w has a Laplacian distribution then the MAP filter becomes an adaptive soft thresholding filter (STF). The hypotheses for this type of marginal MAP filter are:

$$p_w(w) = \left(1/\sqrt{2}\sigma\right) \cdot e^{-\frac{\sqrt{2}|w|}{\sigma}} \text{ and } p_n(n) = \left(1/\sqrt{2\pi}\sigma\right) \cdot e^{-\frac{n^2}{2\sigma_n^2}} \tag{22}$$

The MAP filter equation (4) becomes:

$$\hat{w}(y) = \underset{w}{\mathrm{argmax}}\left\{\ln\left(1/2\sqrt{\pi}\sigma\sigma_n\right) - (y-w)^2 / 2\sigma_n^2 - \sqrt{2}|w|/\sigma\right\}. \tag{23}$$

To maximize the argument of the right hand side, the following equation must be solved:

$$d/dw\left(\ln\left(1/2\sqrt{\pi}\sigma\sigma_n\right) - (y-w)^2 / 2\sigma_n^2 - \sqrt{2}|w|/\sigma\right) = 0 \iff$$
$$\iff (y-w)/\sigma_n^2 - \left(\sqrt{2}/\sigma\right)\mathrm{sgn}(w) = 0 \tag{24}$$

For $w>0$ it becomes:

$$(y-w)/\sigma_n^2 - \sqrt{2}/\sigma = 0 \iff w = y - \sqrt{2}\sigma_n^2/\sigma \tag{25}$$

For $w<0$ the equation (24) becomes:

$$(y - w) / \sigma_n^2 + \sqrt{2} / \sigma = 0 \;\Leftrightarrow\; w = y + \sqrt{2}\sigma_n^2 / \sigma \qquad (26)$$

The condition $w>0$ implies the condition $y > \sqrt{2}\sigma_n^2 / \sigma$ and the condition $w<0$ implies the condition $y < -\sqrt{2}\sigma_n^2 / \sigma$. Taking into account the fact that any real number can be expressed as $y = \mathrm{sgn}(y) \cdot |y|$, the solution of the equation (24) can be put in the following form:

$$\hat{w} = \begin{cases} \mathrm{sgn}\, y\left(|y| - \sqrt{2}\sigma_n^2 / \sigma\right), & |y| < \sqrt{2}\sigma_n^2 / \sigma \\ 0, & |y| > \sqrt{2}\sigma_n^2 / \sigma \end{cases} \qquad (27)$$

equivalent with the final form:

$$\hat{w} = \mathrm{sgn}\, y\left(|y| - \sqrt{2}\sigma_n^2 / \sigma\right)_+ \qquad (28)$$

where:

$$(X)_+ = \begin{cases} X, & \text{for} \quad X > 0 \\ 0, & \text{otherwise} \end{cases}. \qquad (29)$$

This MAP filter is a STF with the threshold's value equal to $\sqrt{2}\sigma_n^2 / \sigma$. Because the quantity σ varies from subband to subband, the threshold's value is variant. In this respect the last MAP filter can be considered adaptive. Of course the two variances in equation (28) could be estimated using equations (16) and (19).

2.4.1.2.3 Inter-scale dependence of wavelet coefficients

The wavelet coefficients are characterized by interscale dependence.

The cross-correlation of two wavelet coefficients belonging to the 2D DWT of an image f, located in the same subband k at the scales m_1 and $m_2 = m_1 + q$ and having the geometrical coordinates $(n_1 = 2^q n_1', p_1 = 2^q p_1')$ and (n_2, p_2) respectively is given by the following relation:

$$R_{f^{D^k_{m_1}} f^{D^k_{m_2}}}\left(2^q n'_1 - n_2, 2^q p'_1 - p_2\right) = 2^{2m_1+q} R_f\left(2^{m_1+q}(n_2 - n_1'), 2^{m_1+q}(p_2 - p_1')\right) \\ * R_{\psi^k}(n_2 - n_1', p_2 - p_1'). \qquad (30)$$

which represents an inter-scale and intra-band dependency. If the mother wavelet ψ^k generates by translations and dilations an **orthogonal** basis of $L^2(R^2)$ then its autocorrelation has the following property:

$$R_{\psi^k}(n, p) = \delta[n, p] \qquad (31)$$

and the expression of the inter-scale and intra-band dependency of the coefficients cross-correlation becomes:

$$R_{f^{D^k_{m_1}} f^{D^k_{m_2}}}\left(2^q n'_1 - n_2, 2^q p'_1 - p_2\right) = 2^{2m_1+q} R_f\left(2^{m_1+q}(n_2 - n_1'), 2^{m_1+q}(p_2 - p_1')\right). \qquad (32)$$

This cross-correlation is function of the autocorrelation of the input signal. If we refer to pairs of wavelet coefficients located at two consecutive decomposition levels ($q=1$, $m_2 = m_1+1$) at the same coordinates ($n_1 = 2n_2$, $p_1 = 2p_2$) which are named parent coefficient ($_fD_{m_1+1}^k(n_2,p_2)$) and child coefficient ($_fD_{m_1}^k(n_1,p_1)$) the expression of their inter-scale dependence becomes:

$$R_{_fD_{m_1}^k\,_fD_{m_1+1}^k}(n_2,p_2) = 2^{2m_1+1}R_f(0,0) \tag{33}$$

which means that the child and the parent coefficient are correlated. So, if the magnitude of the parent coefficient is large (small) then the magnitude of the child coefficient is also large (small). Taking into consideration that the computation of the HWT reduces at the computation of the 2D DWTs of four related images f, $H_x\{f\}$, $H_y\{f\}$ and $H_y\{H_x\{f\}\}$, as can be seen in figure 8, a similar inter-scale dependence can be observed in the case of the pair of parent and child HWT coefficients:

$$R_{z_{+i}z_{+i}}[m_1,m_1+1,k,n_2,p_2] = 2^{2m_1+1}\{R_{Hx}(0,0) + R_{HxHy}(0,0) + R_{HyHx}(0,0) + R_{Hy}(0,0)\}. \tag{34}$$

The MAP filters which take into account this dependence are multivariate and have better performance. Some bivariate probability density functions are constructed starting from the Gaussian scale mixture (GSM) statistical model [Selesnick, 2008].

2.4.1.2.4 The GSM model

The construction of the bivariate pdf can be done with the aid of Gaussian Scale Mixtures (GSM). This simple statistical model has been used to model natural signals such as speech and more recently the wavelet coefficients of natural images. The model is given in equation (35). It assumes that each vector of coefficients **w** is specified by a stationary bivariate zero mean Gaussian process **x** and a spatially fluctuating variance z.

$$\mathbf{w} = \sqrt{z}\cdot\mathbf{x}, \quad z \in \mathrm{R}, \quad \mathbf{w},\mathbf{x} \in \mathrm{R}^d \tag{35}$$

The multiplier z is usually a function of the surrounding coefficient values (like the local variance of the coefficients within the same scale or a more complex function of the neighboring coefficients within the same and adjacent scales). The result is always leptokurotic (kurtosis ≥ 3), its distribution having long tails. The MMSE estimate with such priors takes the form of a locally adaptive Wiener-like estimator. Usually the number of elements of the vectors **x** and **w** is $d=2$. To model the self-reinforcing property of the coefficients, z must be slowly varying but it does not need to be symmetric in all directions. It has been shown that for slowly varying z this model can successfully simulate the high kurtosis and longer tails of the marginal distributions. The stationary portion of the model **x** is Gaussian distributed over a small neighborhood of wavelet coefficients. It is generally assumed that z varies slowly enough to be considered constant over that neighborhood of coefficients. Under this assumption the model is now a particular form of a spherically invariant random process called a GSM. For a small neighborhood of coefficients at nearby spatial locations and scale, a GSM vector **w** is the product of two independent random variables: a positive scalar z referred to as the hidden multiplier or mixing variable and a Gaussian random vector **x**. The pdf of the Gaussian vector **x** is given by:

$$p_{\mathbf{x}}(\mathbf{x}) = \left[1 / \left(2\pi\sigma^2 \right)^{d/2} \right] \cdot e^{-\frac{\|x\|^2}{2\sigma^2}} \tag{36}$$

(see (12)). Setting $a = \sqrt{z}$, we obtain $\mathbf{w} = a \cdot \mathbf{x}$ and the pdf of the random vector $\mathbf{w}$ is given by:

$$p_{\mathbf{w}}(\mathbf{w}) = \int_0^\infty p_a(a) \cdot \left(1 / a^d \right) \cdot p_{\mathbf{x}}(\mathbf{w}/a) da \tag{37}$$

Tacking into account the relation of a and z, the pdf of a can be expressed on the basis of the pdf of z:

$$p_a(a) = p_z(z) / (da / dz) = p_z\left(a^2\right) / (1 / 2a) = 2a \cdot p_z\left(a^2\right) \tag{38}$$

Substituting (38) into (37), the expression of the pdf of $\mathbf{w}$ becomes:

$$p_{\mathbf{w}}(\mathbf{w}) = \int_0^\infty 2a p_z\left(a^2\right) \cdot \left(1 / a^d \right) \cdot p_x(\mathbf{w}/a) da \tag{39}$$

It remains to specify the prior probability function $p_z(z)$ for the multiplier z. Some propositions of prior probability functions are made in [Selesnick, 2008]. One of these propositions is the Gamma law:

$$p_z(z) = \beta^\alpha / \Gamma(\alpha) \cdot z^{\alpha-1} \cdot e^{-\beta z} \text{ with } \alpha = \beta = (d+1) / 2 \tag{40}$$

Substituting (40) into (39), the expression of the pdf of $\mathbf{w}$ becomes:

$$^1p_{\mathbf{w}}(\mathbf{w}) = \left[2(\beta)^\alpha / \Gamma(\alpha) \right] \int_0^\infty a \cdot a^{2(\alpha-1)} \cdot e^{-\beta a^2} \cdot a^{-d} \cdot \left(2\pi\sigma^2 \right)^{-\frac{d}{2}} \cdot e^{-\frac{\|\mathbf{w}\|^2}{2a^2\sigma^2}} da \tag{41}$$

Finally:

$$^1p_{\mathbf{w}}(\mathbf{w}) = \left(2 / \Gamma\left(\frac{d+1}{2}\right) \right) \cdot \left[(d+1) / 2 \right]^{\frac{d+1}{2}} \cdot \left(2\pi\sigma^2 \right)^{-\frac{d}{2}} \cdot \sqrt{\left\{ \pi / \left[(d+1) / 2 \right] \right\}} \cdot e^{-\frac{\sqrt{d+1}}{\sigma} \cdot \|\mathbf{w}\|} \tag{42}$$

This is a d-dimensional spherically-contoured multivariate pdf [Selesnick, 2008]. For $d=2$, this pdf is bivariate:

$$^1p_{\mathbf{w}}(\mathbf{w}) = \left(3 / 2\pi\sigma^2 \right) \cdot e^{-\frac{\sqrt{3}}{\sigma} \cdot \sqrt{w_1^2 + w_2^2}}. \tag{43}$$

With the aid of this bivariate distribution the bishrink MAP filter [Sendur&Selesnick, 2002] can be constructed. This construction will be explained in the following section. For $d=1$, the pdf in (43) is univariate:

$$_1 p_w(w) = \left(\sqrt{2} / \sigma \right) \cdot e^{-\frac{\sqrt{2}}{\sigma} \cdot |w|} \tag{44}$$

This univariate pdf is of the form of the Laplace law; see the hypotheses of the adaptive STF, (22). In consequence the GSM hypothesis, even for the case of a unique scale, is useful for modeling the repartition of the wavelet coefficients. Other proposition of prior probability function made in [Selesnick, 2008] is the exponential $p_z(z) = e^{-z}$ for $z \geq 0$. The GSM model was also used for the conception of one of the best denoising methods [Portilla et al., 2003]. The prior probability function proposed in this reference is $p_z(z) = 1 / z,$ for $z \geq 0$. It must be remarked that strictly speaking this is not a pdf. Substituting this function in (39) and supposing that the pdf of the Gaussian vector is that given in (36) it can be written:

$$_4 p_{\mathbf{w}}(w_1, w_2) = -\frac{1}{\pi \|\mathbf{w}\|^2} \cdot e^{-\frac{\|\mathbf{w}\|^2 t^2}{2\sigma^2}} \Big|_0^\infty = \frac{1}{\pi \|\mathbf{w}\|^2} = \frac{1}{\pi \left(w_1^2 + w_2^2 \right)}. \tag{45}$$

It results a third spherically-contoured bivariate pdf. A last bivariate pdf for the wavelet coefficients was proposed in [Achim&Kuruoglu, 2005]:

$$_5 p_{\mathbf{w}}(w_1, w_2) = \frac{\gamma}{2\pi \left(w_1^2 + w_2^2 + \gamma^2 \right)^{\frac{3}{2}}}. \tag{46}$$

Using one of these models, in [Selesnick, 2008] is conceived a bivariate MAP filter called bishrink.

2.4.1.2.5 The bishrink filter

The noise is assumed i.i.d. Gaussian,

$$p_{\mathbf{n}}(\mathbf{n}) = \frac{1}{2\pi\sigma_n^2} \cdot e^{-\frac{n_1^2 + n_2^2}{2\sigma_n^2}}. \tag{47}$$

The model of the noise-free image is given in (43):

$$_1 p_{\mathbf{w}}(\mathbf{w}) = \frac{3}{2\pi\sigma^2} \cdot e^{-\frac{\sqrt{3}}{\sigma}\sqrt{w_1^2 + w_2^2}} \tag{}$$

a heavy tailed distribution. Substituting these two pdfs in the equation of the MAP filter (4) this equation becomes:

$$_1 \hat{\mathbf{w}}(\mathbf{y}) = \underset{\mathbf{w}}{\operatorname{argmax}} \left\{ \ln \frac{3}{4\pi^2\sigma^2\sigma_n^2} - \frac{(y_1 - w_1)^2}{2\sigma_n^2} - \frac{(y_2 - w_2)^2}{2\sigma_n^2} - \frac{\sqrt{3}}{\sigma}\sqrt{w_1^2 + w_2^2} \right\}. \tag{48}$$

The system of equations that gives the maximum of the right hand side of the last equation is:

$$\begin{cases} \dfrac{d}{dw_1}\left(\ln \dfrac{3}{4\pi^2\sigma^2\sigma_n^2} - \dfrac{(y_1-w_1)^2}{2\sigma_n^2} - \dfrac{(y_2-w_2)^2}{2\sigma_n^2} - \dfrac{\sqrt{3}}{\sigma}\sqrt{w_1^2+w_2^2} \right) = 0 \\[3mm] \dfrac{d}{dw_2}\left(\ln \dfrac{3}{4\pi^2\sigma^2\sigma_n^2} - \dfrac{(y_1-w_1)^2}{2\sigma_n^2} - \dfrac{(y_2-w_2)^2}{2\sigma_n^2} - \dfrac{\sqrt{3}}{\sigma}\sqrt{w_1^2+w_2^2} \right) = 0 \end{cases} \qquad (49)$$

or:

$$\begin{cases} \dfrac{y_1-w_1}{\sigma_n^2} - \dfrac{\sqrt{3}}{\sigma}\cdot\dfrac{w_1}{\sqrt{w_1^2+w_2^2}} = 0 \\[3mm] \dfrac{y_2-w_2}{\sigma_n^2} - \dfrac{\sqrt{3}}{\sigma}\cdot\dfrac{w_2}{\sqrt{w_1^2+w_2^2}} = 0 \end{cases} \qquad (50)$$

The system can be put in the following form:

$$\begin{cases} \dfrac{y_1}{\sigma_n^2} = \dfrac{\sqrt{3}}{\sigma}\cdot\dfrac{w_1}{\sqrt{w_1^2+w_2^2}} + \dfrac{w_1}{\sigma_n^2} \\[3mm] \dfrac{y_2}{\sigma_n^2} = \dfrac{\sqrt{3}}{\sigma}\cdot\dfrac{w_2}{\sqrt{w_1^2+w_2^2}} + \dfrac{w_2}{\sigma_n^2} \end{cases}$$

or equivalently:

$$\begin{cases} w_1 = \dfrac{\sigma\sqrt{w_1^2+w_2^2}}{\sigma\sqrt{w_1^2+w_2^2}+\sqrt{3}\sigma_n^2}\,y_1 \\[3mm] w_2 = \dfrac{\sigma\sqrt{w_1^2+w_2^2}}{\sigma\sqrt{w_1^2+w_2^2}+\sqrt{3}\sigma_n^2}\,y_2 \end{cases} \qquad (51)$$

Computing the square of each equation it results:

$$\begin{cases} w_1^2 = \dfrac{\sigma^2\left(w_1^2+w_2^2\right)}{\left[\sigma\sqrt{w_1^2+w_2^2}+\sqrt{3}\sigma_n^2 \right]^2}\,y_1^2 \\[3mm] w_2^2 = \dfrac{\sigma^2\left(w_1^2+w_2^2\right)}{\left[\sigma\sqrt{w_1^2+w_2^2}+\sqrt{3}\sigma_n^2 \right]^2}\,y_2^2 \end{cases} \qquad (52)$$

By adding the two equations it can be obtained:

$$w_1^2+w_2^2 = \dfrac{\sigma^2\left(w_1^2+w_2^2\right)}{\left[\sigma\sqrt{w_1^2+w_2^2}+\sqrt{3}\sigma_n^2 \right]^2}\left(y_1^2+y_2^2\right) \iff \sqrt{w_1^2+w_2^2} = \left(\sqrt{y_1^2+y_2^2} - \sqrt{3}\,\dfrac{\sigma_n^2}{\sigma} \right)_+ \qquad (53)$$

Substituting this result in the two equations of the system in (52) it can be written:

$$
\begin{cases}
{}^{1}\hat{w}_1 = \dfrac{\left(\sqrt{y_1^2 + y_2^2} - \sqrt{3}\,\dfrac{\sigma_n^2}{\sigma}\right)_+}{\sqrt{y_1^2 + y_2^2}}\, y_1 \\[4mm]
{}^{1}\hat{w}_2 = \dfrac{\left(\sqrt{y_1^2 + y_2^2} - \sqrt{3}\,\dfrac{\sigma_n^2}{\sigma}\right)_+}{\sqrt{y_1^2 + y_2^2}}\, y_2
\end{cases}
\tag{54}
$$

So the input-output relation of the bishrink filter is:

$$
{}_1\widehat{w}_1 = \frac{\left(\sqrt{y_1^2 + y_2^2} - \dfrac{\sqrt{3}\sigma_n^2}{\sigma}\right)_+}{\sqrt{y_1^2 + y_2^2}}\, y_1
\tag{55}
$$

It can be observed that the bishrink filter is an estimator of the adaptive STF type. In this case the threshold's value is $t = \dfrac{\sqrt{3}\sigma_n^2}{\sigma}$. This estimator requires prior knowledge of the noise variance and of the marginal variance of the clean image for each wavelet coefficient. These quantities can be estimated using the equations (16) and (19). The sensitivity of the bishrink filter with the estimation of the noise standard deviation $\hat{\sigma}_n$ can be computed with the relation:

$$
S_{\widehat{w}_1}^{\hat{\sigma}_n} = \frac{d\widehat{w}_1}{d\hat{\sigma}_n} \cdot \frac{\hat{\sigma}_n}{\hat{w}_1}
$$

The input-output relation of the bishrink filter (55) can be put in the following form:

$$
\hat{w}_1 = \begin{cases}
\dfrac{\sqrt{y_1^2 + y_2^2} - \dfrac{\sqrt{3}\hat{\sigma}_n^2}{\hat{\sigma}}}{\sqrt{y_1^2 + y_2^2}}\, y_1, & \text{if } \sqrt{y_1^2 + y_2^2} > \dfrac{\sqrt{3}\hat{\sigma}_n^2}{\hat{\sigma}} \\[4mm]
0, & \text{otherwise}
\end{cases}
\tag{56}
$$

So, it can be written:

$$
S_{\widehat{w}_1}^{\hat{\sigma}_n} = \begin{cases}
\dfrac{-2\sqrt{3}\hat{\sigma}_n^2}{\hat{\sigma}\sqrt{y_1^2 + y_2^2} - \sqrt{3}\hat{\sigma}_n^2}, & \text{if } \sqrt{y_1^2 + y_2^2} > \dfrac{\sqrt{3}\hat{\sigma}_n^2}{\hat{\sigma}} \\[4mm]
0, & \text{otherwise}
\end{cases}
\tag{57}
$$

The absolute value of this sensitivity is inversely proportional to $\hat{\sigma}_n$. When the value of the estimation of the noise standard deviation is higher then the performance of the bishrink filter is poorer.

Another very important parameter of the bishrink filter is the local estimation of the marginal variance of the noise-free image $\hat{\sigma}$. The sensitivity of the estimation $\hat{w}_1$ with $\hat{\sigma}$ is given by:

$$S^{\hat{\sigma}}_{\hat{w}_1} = \begin{cases} \dfrac{\sqrt{3}\hat{\sigma}_n^2}{\hat{\sigma}\sqrt{y_1^2 + y_2^2} - \sqrt{3}\hat{\sigma}_n^2}, & \text{if } \sqrt{y_1^2 + y_2^2} > \dfrac{\sqrt{3}\hat{\sigma}_n^2}{\hat{\sigma}} \\ 0, & \text{otherwise} \end{cases} \tag{58}$$

This is a decreasing function of $\hat{\sigma}$. The precision of the estimation based on the use of the bishrink filter decreases with the decreasing of $\hat{\sigma}$. Similar sensitivity analyses can be accomplished for the zero order Wiener filter or for the adaptive soft-thresholding filter, concluding that their worst behavior corresponds to the homogeneous regions of their noise-free input image component.

Secondly, the local variance of a pixel gives some information about the frequency content of the region to which the considered pixel belongs. If the pixels of a given region have low local variances then the considered region contains low frequencies. If these pixels have high local variances then the considered region contains high frequencies.

The bishrink is a local bivariate MAP filter. Its performance depends on the quality of the estimation of a parameter, the local variance of the noiseless component of the acquired image. The quality of this estimate depends on the shape and the size of the estimation window. These estimation windows have different shapes in subbands with different preferential orientations highlighting the better directional selectivity of DTCWT and HWT versus the DWT.

Other MAP filters can also be considered. A MAP filter constructed on the basis of a bivariate Cauchy model is described in [Achim&Kuruoglu, 2005]. The Pearson statistical model is exploited for the construction of the marginal MAP filter presented in [Foucher et al., 2001]. The model of generalized Gaussian (GG) is used in [Argenti et al., 2006].

2.5 Despecklisation systems

We will compare in the following the classical despecklisation systems with some modern denoising systems conceived for the reduction of speckle noise in SONAR images based on complex WTs, namely the 2D DT CWT and the HWT.

The modern systems have the architecture presented in figure 12. The block named Sensitivity reduction corrects the drawbacks of the additive noise denoising kernel. One of the disadvantages of homomorphic denoising methods is the introduction of an undesirable bias. The expectations of the result and of the noiseless component of the acquired image are different. Their difference is given by the bias already mentioned. The proposed despecklisation system corrects this bias with the aid of two mean computation systems. The correction is based on the property of the speckle noise to have unitary expectation. The first mean computation system in figure 1 estimates the mean of the acquired image which is equal with the mean of its noise-free component (because the speckle has unitary mean). The second mean computation system in figure 12 computes the mean of the image at the output of the Sensitivity reduction block. This value is extracted and the mean of the noiseless component of the acquired image is added.

Both additive noise denoising kernels which exploit the 2D DT CWT and the HWT use the bishrink filter associated with the corresponding complex WT. The architecture of the corresponding Sensitivity reduction blocks is different for the two complex WTs.
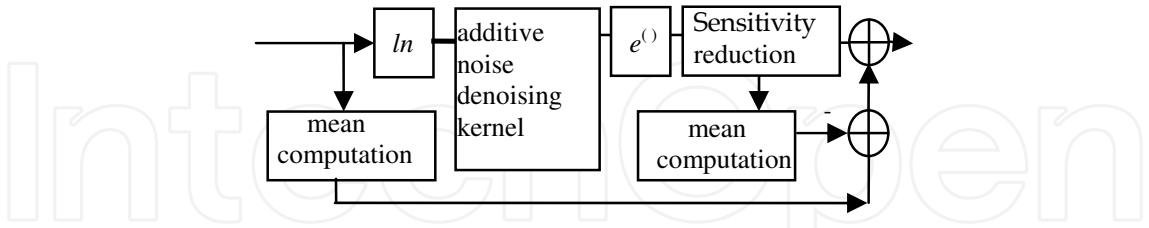

Fig. 12. The architecture of the proposed denoising system. The mean correction mechanism and the additive noise denoising kernel are highlighted.

The bishrink filter can be used for despecklisation in the wavelets domain because its statistical model for the noise is appropriate as can be seen from the following experiment. The speckle can be modeled using a Rayleigh distribution with unitary mean. It is obtained computing the square root of a sum of squares of two white Gaussian noises having the same variance. The first image of figure 13 contains a normalized representation of the pdf in equation (43) particularized for a given variance of the noise. The second image of figure 13 represents the normalized bivariate histogram of the HWT coefficients **of the logarithm of the noise.** It was obtained considering the HWT coefficients z_{+r} corresponding to horizontal details from the first two decomposition levels. The similarity of the surfaces from the two images in figure 13 proves the validity of the bivariate noise statistical model used for the construction of the bishrink filter and the possibility to use this filter in despecklisation applications.
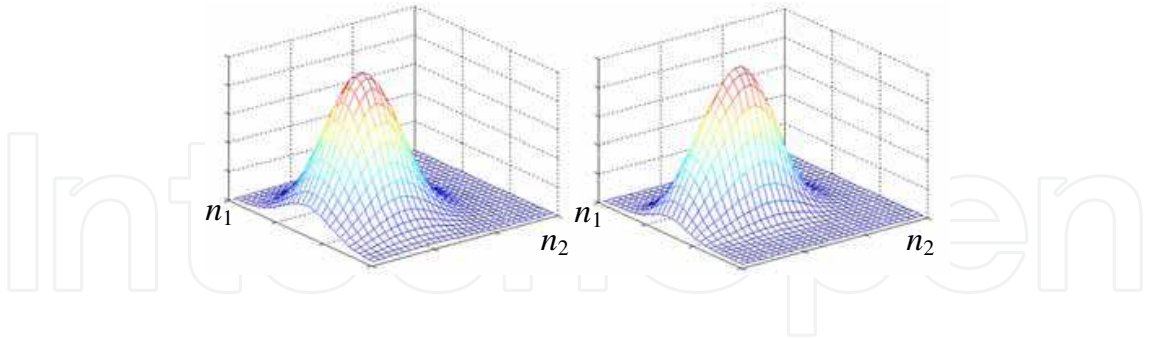
Fig. 13. The representation of the pdf in eq. (49) (left) and the corresponding bivariate histogram (right).

2.6 Simulations results

We present two types of simulation results: for synthesized speckle noise and for real SONAR images. The performance of the simulation results reported in this chapter is appreciated on the basis of some quality measures. The first one is the peak signal to noise ratio (PSNR) which is defined in the following. Let s and $\hat{s}$ denote the clean and the denoised images. The root mean square (rms) of the approximation error is computed by:

$$\varepsilon = \sqrt{\frac{1}{N_p} \sum_q \left(s_q - \hat{s}_q\right)^2}$$

where N_p is the number of pixels. The PSNR in dB is given by:

$$\text{PSNR} = 20 \log_{10} \left(\frac{255}{\varepsilon}\right)$$

Because its computation requires the knowledge of s the PSNR is computed in the experiments associated with synthesized speckle noise. Another quality measure is represented by the method's noise. For multiplicative noise (as the speckle is) the method's noise is defined by the ratio between the acquired image and the denoising result. This noise must be as similar as possible with the noise which perturbed the noiseless component of the acquired image. As the PSNR, the method noise can be appreciated only in the experiments associated with synthesized speckle. A third measure of quality of the denoising of a homogeneous region is given by the enhancement of the equivalent number of looks (ENL):

$$ENL = \left(\frac{\text{mean}}{\text{standard deviation}}\right)^2 .$$

The enhancement of ENL is computed as the ratio of the output and input ENLs of the same region. This is a quality measure which can be appreciated in the case of real SONAR images as well. We have used two types of synthesized speckle. The first type is synthesized using a Rayleigh distribution with unitary mean and it is associated with the image Lena. The second type is synthesized using the method proposed in [Walessa&Datcu, 2000] and is associated with the test image presented in figure 14 [Walessa&Datcu, 2000].
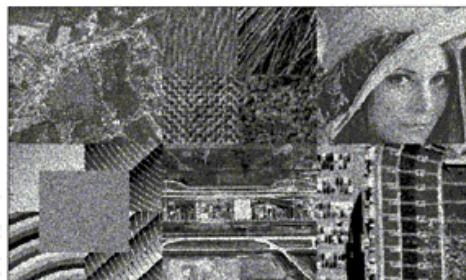
Fig. 14. A test image obtained by the multiplication of a mosaic of real and synthesized images with the speckle noise generated in [Walessa&Datcu, 2000].

To run these simulations on real SONAR images we have used a database obtained from IFREMER Brest France. We are thankful for this opportunity. Besides these three objective quality measures, we considered the visual aspect of the results as well.

2.6.1 Synthesized images

We have applied first the classical despecklisation methods to the test image in figure 14 obtaining the results presented in figure 15. The corresponding filters are indexed with two indices, the first one specifying the size of the analysis window (for example 7 for a

rectangular window with size 7×7) and the second one the number of looks of the image treated (1 in all the three cases).
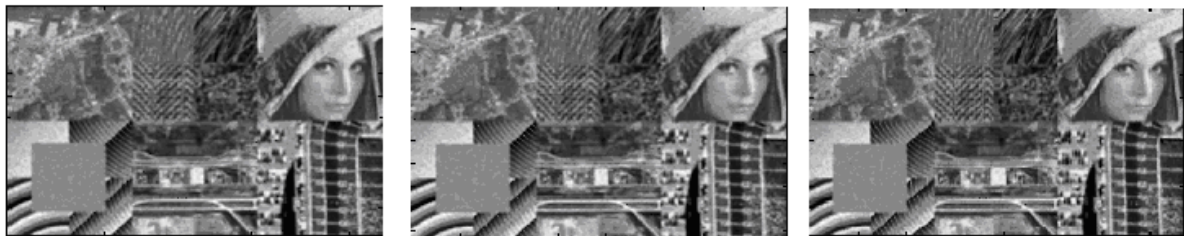

Fig. 15. A comparison of the classical despecklisation filters; from left to right: Kuan 9-1 , Lee 7-1, Frost 5-1.

The PSNRs obtained separating the sub-image Lena from the test image and from the results in figure 15 are indicated in Table I and compared with the results obtained by applying the denoising methods which associates the bishrink filter with the 2D DT CWT (fifth column) and with the HWT (sixth column) respectively.

Noisy	Lee	Frost	Kuan	2D DT CWT	HWT
21.4	27.2	27.0	28.1	*31.4*	31.9

Table 1. The PSNRs of different speckle denoising methods (in dB).

The superiority of the denoising methods acting in the wavelet domain is obvious. The comparison in figure 16 permits the appreciation of the visual aspect of the results of the methods based on 2D DT CWT and HWT for the treatment of the test image in figure 14. These results are compared in figure 16 with the result of another despecklisation method applied in the spatial domain [Walessa&Datcu, 2000]. The superiority of the directional selectivity of the methods based on complex wavelets can be observed comparing the interior of the regions highlighted in yellow. Indeed the methods based on wavelets conserve better the details of the hat. The result with the best visual aspect in figure 16 corresponds to the utilization of the HWT. In figure 17 are compared the results of three different methods based on wavelets. The first two despecklisation methods are those based on 2D DT CWT and HWT and the third one was proposed in [Argenti et al., 2006] and is based on the association of the 2D UDWT with a MAP filter. The 2D UDWT is computed either with the aid of the Daubechies mother wavelets with eight vanishing moments, db8 or with the pair of biorthogonal mother wavelets bior9.7. The first denoising algorithm proposed in [Argenti et al., 2006] performs a local linear minimum mean square error (LLMMSE) filtering in the UDWT domain. The second one uses a MAP filter constructed supposing that the noise-free wavelet coefficients and the wavelet coefficients of the noise are distributed according to Generalized Gaussian Distributions.

The parameters of those pdfs are estimated for each pixel of the input image. The corresponding MAP filter equation is solved with the aid of numerical methods. All the three results in figure 17 have a good visual aspect. The methods based on complex wavelets (2D DT CWT and HWT) prove a better output PSNR, a better directional selectivity, a better treatment of the contours and textures and a better contrast preservation but the method based on 2D UDWT treats better the homogeneous regions. The method's noise corresponding to the use of 2D DT CWT is quite identical with the original noise (compare images (b) and (d)) some differences appearing in the dark regions of the image Lena.
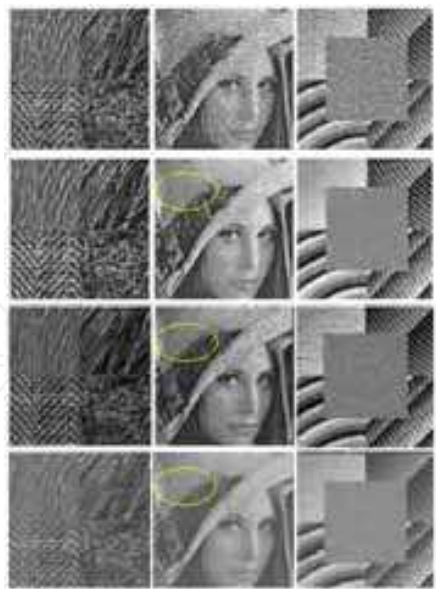
Fig. 16. A comparison of the visual aspect of the results of three despecklisation methods;
From up to bottom: noisy sub-images, results obtained applying the method in
[Walessa&Datcu, 2000], results obtained applying the method in [Ifremer, 2010] and results
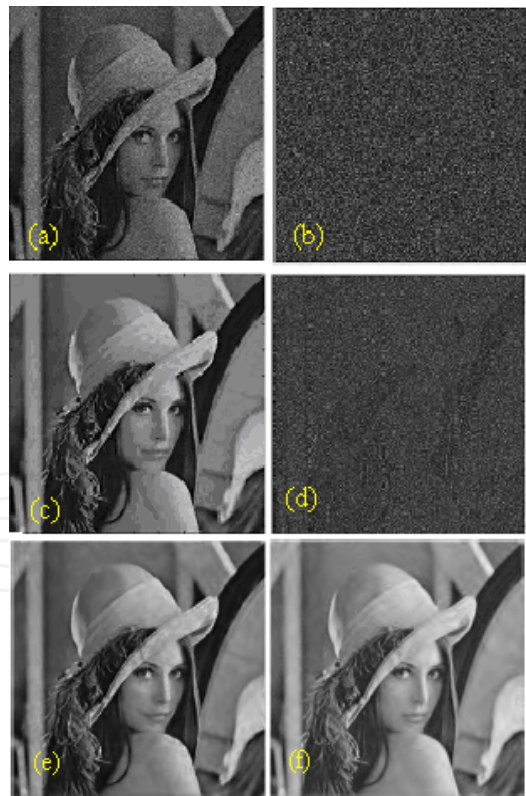obtained applying the method based on the HWT.

Fig. 17. A comparison of three despecklisation methods acting in the wavelets domain; (a)
noisy image (PSNR=21.4 dB), (b) speckle noise distributed following a Rayleigh law with
unitary mean, (c) result obtained with the method based on 2D DT CWT (PSNR=31.4 dB), (d)
2D DT CWT method's noise, (e) result obtained with the method based on HWT (PSNR=32.5
dB), (f) result obtained with the method in [Argenti et al., 2006] (PSNR=31.1 dB).
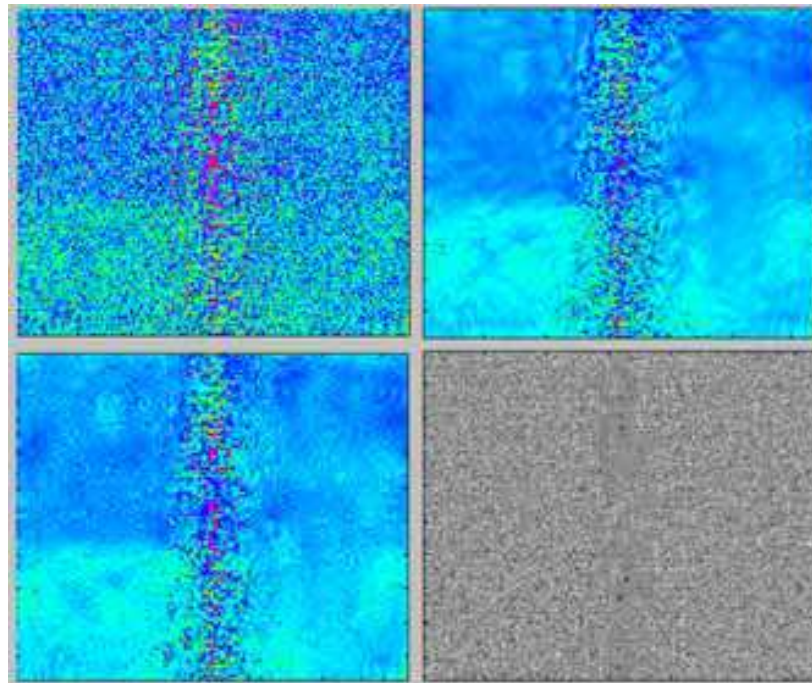
Fig. 18. A comparison of the despecklisation methods based on 2D DT CWT and HWT. From left to right and up to bottom; acquired SONAR image, result of the despecklisation method based on 2D DT CWT, result of the despecklisation method based on HWT, 2D DT CWT method's noise.

2.6.2 Real images

In figure 18 is made a comparison of the despecklisation methods based on 2D DT CWT and HWT applied to a very difficult SONAR image. The first picture in figure 18 represents the acquired SONAR image. It is very difficult because it has small size (200×320) and because the relief of the sea floor is flat in the region considered. So, all the pixels have intensities of similar values. The image was artificially colored, to see better the small intensity differences. Even the specular region can be observed with difficulty in this picture. This image is very noisy. It can be observed, analyzing the results of denoising, a demarcation line between two regions (the blue one and the green one) with pixels having different intensities. The difference between the intensities of the pixels belonging to the two regions is smaller than 1 dB. So, the proposed denoising method increases the discrimination capability of the analyst. Another consequence of the denoising based on wavelets is the better separation of the specular region from the rest of the scene. It can be also observed that a great amount of noise was eliminated by the proposed denoising methods. Comparing the second and the third pictures in figure 18, it can be noticed that the result of the despecklisation method based on the 2D DT CWT is over smoothed. So, the despecklisation method based on HWT seems to be the best choice. The comparison of the despecklisation methods based on 2D DT CWT and HWT is continued in figure 19, where other two SONAR images are considered. On the first column are represented the row SONAR images, on the second column are represented the results obtained applying the despecklisation method based on 2D DT CWT and on the last column are represented the results obtained applying the despecklisation method based on HWT. Analyzing figure 19, it can be observed that the two despecklisation methods based on wavelets are equivalent

from the visual aspect point of view. Finally, we compare in figure 20 the two denoising methods based on 2D DT CWT and HWT respectively using a SONAR image containing a higher amount of information. The performance obtained by the two despecklisation methods based on wavelets for homogeneous regions is certificated by the important enhancements of ENL obtained considering a region of 120×1000 pixels. The gain in performance of the method based on HWT can be explained by the superiority of HWT versus 2D DT CWT in despecklization applications.
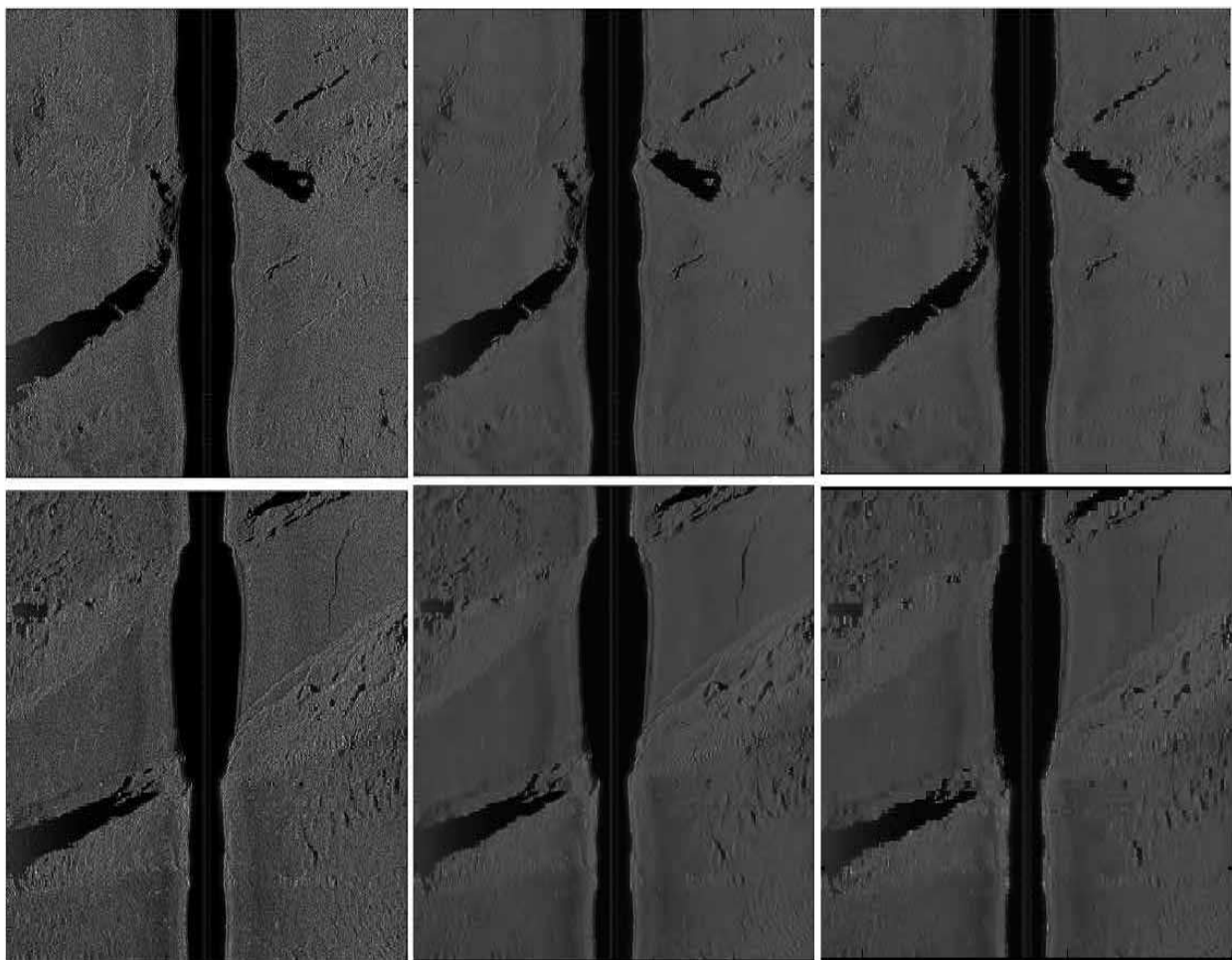
Fig. 19. A comparison of two despecklisation methods based on wavelets; First column: raw images, Second column: results obtained applying the despecklisation method based on 2D DT CWT, Third column: results obtained applying the despecklisation method based on HWT.

3. Conclusion

This book is dedicated to SONAR systems. Despite the actual proliferation of this type of images, there are not numerous publications dealing with their denoising. In this chapter was presented the particular case of SONAR images starting with an overview of speckle removal techniques both in the spatial domain and in the wavelet domain. We have proved by simulations the superiority of the methods applied in the wavelet domain. These methods were classified according to the type of the wavelet transform used: 2D DWT, 2D
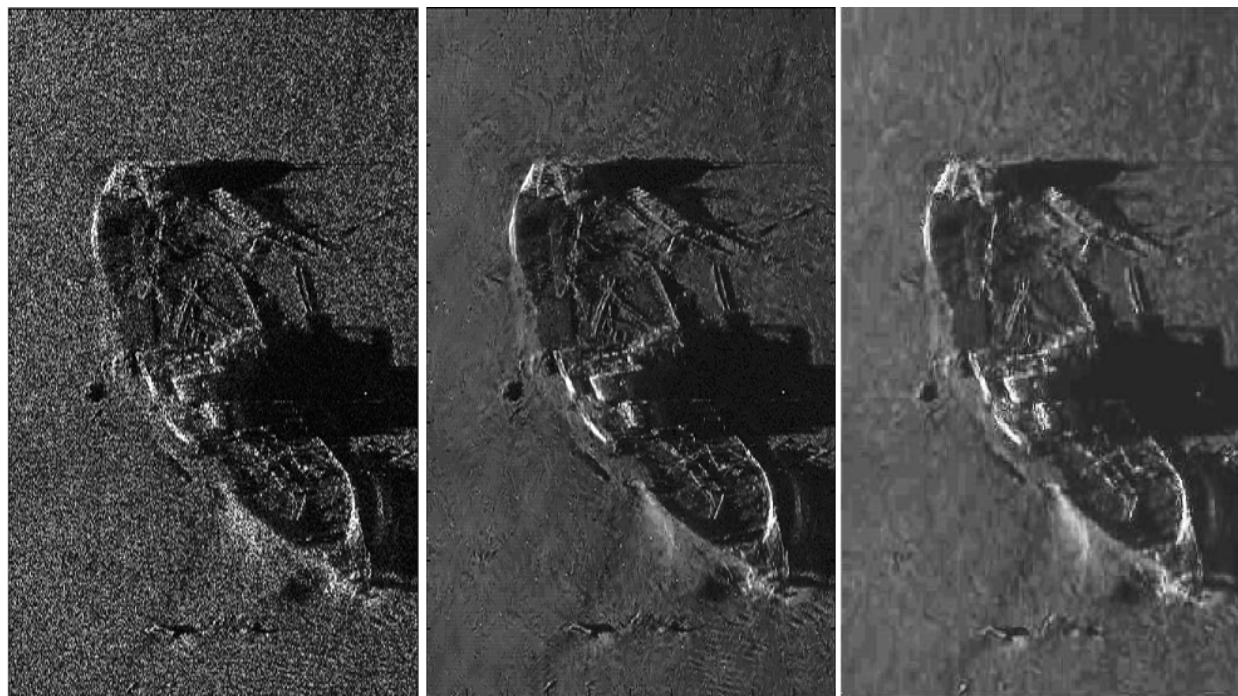
Fig. 20. Left: sea-bed sonar Swansea image (we are thankful to GESMA for providing this image, ENL=3.4), Middle: result of the method based on 2D DT CWT (ENL=102), Right: result of the method based on HWT (ENL=150).

UDWT, 2D DT CWT and HWT. In the case of the 2D DT CWT and HWT, we have used homomorphic filtering techniques and applied the bishrink filter in the 'additive noise denoising kernel' block, in figure 12. The proposed algorithms use two of the best WTs, the 2D DT CWT and the HWT and a very good MAP filter which can be associated for despecklisation purposes. The undesirable bias introduced by the homomorphic methods is corrected using a clever combination of two expectation computation blocks.

The results obtained were satisfactory, especially those in which HWT with Biorthogonal 9/7 as mother wavelet was associated with the bishrink filter, followed by a supplementary correction applied to homogeneous areas. We have proved by simulation that the HWT is a better choice than the DWT, the UWT or the DT CWT for SONAR images despecklisation. The denoising method based on HWT outperforms other remote sensing images denoising methods from the visual aspect (it preserves better the contrast of the noiseless component of the image which must be denoised), the PSNR enhancement and the enhancement of ENL points of view. It is faster than the other despecklisation methods as well.

4. Acknowledgment

5. References

[Ifremer, 2010] http://www.ifremer.fr/fleet/acous_sism/sonarscope/index.html.

[Abry, 1994] Abry P. (1994), *Transformées en ondelettes-Analyses multirésolution et signaux de pression en turbulence.* PhD thesis, Université Claude Bernard, Lyon, France.

[Achim&Kuruoglu, 2005] Achim A. and Kuruoglu E. E. (2005), Image Denoising Using Bivariate α-Stable Distributions in the Complex Wavelet Domain, *IEEE Sig. Proc. Let.*, 12 (1), January 2005, pp. 17-20, ISSN 1070-9908.

[Argenti et al., 2006] Argenti F., Bianchi T. and Alparone L. (2006), Multiresolution MAP Despeckling of SAR Images Based on Locally Adaptive Generalized Gaussian PDF Modeling, *IEEE Trans. on Image Proc.*, vol. 15, no. 11, Nov. 2006, pp. 3385-3399, ISSN 1057-7149.

[Argenti et al., 2009] Argenti F., Bianchi T., di Scarfizzi G.M., Alparone L. (2009), LMMSE and MAP Estimators for Reduction of Multiplicative Noise in the Nonsubsampled Contourlet Domain, *Signal Processing*, vol. 89, no. 10, Oct. 2009, pp. 1891−1901, ISSN 0165-1684.

[Buades, 2007] Buades A. (2007), *Image and film denoising by non-local means*, Ph. D. Thesis, Universitat de les Iles Baleares.

[Davenport, 2010] Davenport C., *Commutative Hypercomplex Mathematics*, December 17, 2010, http://home.comcast.net/ cmdaven/hypercplx.htm.

[Donoho&Johnstone, 1994] Donoho D. L. and Johnstone I. M. (1994), Ideal spatial adaptation by wavelet shrinkage, *Biometrika*, 81(3), March 1994, pp. 425-455, ISSN 0006-3444.

[Frost et al., 1982] Frost V. S., Stiles J. A., Shanmugan J. A. and Holtzman J. C. (1982), A Model for Radar Images and Its Application to Adaptive Digital Filtering of Multiplicative Noise, *IEEE Transactions on Pattern Analysis and Machine Intelligence*, Vol. PAMI-4, No. 2, March 1982, pp. 157 - 166 , ISSN 0162-8828.

[Foucher et al., 2001] Foucher S., Benie G. B. and Boucher J.-M., (2001), Multiscale MAP Filtering of SAR images, *IEEE Trans. Ima. Proc.*, vol. 10, no.1, January 2001, pp. 49-60, ISSN 1057-7149.

[Holschneider et al., 1989] Holschneider M., Kronland-Martinet R., Morlet J. and Tchamitchian P. (1989), Wavelets. Time-frequency Methods and Phase Space, chapter *A Real-Time Algorithm for Signal Analysis with the Help of the Wavelet Transform*, pages 289–297, Springer-Verlag, ISBN-10: 3540530142, Berlin, Germany.

[Jalobeanu et al., 2003] Jalobeanu A., Blanc-Féraud L. and Zerubia J., (2003), Natural image modeling using complex wavelets". In *Proc. of SPIE, Wavelets X*, Volume: 5207, 2003, pp. 480-494, ISBN: 9780819450807.

[Katkovnik et al., 2006] Katkovnik V., Egiazarian K. and Astola J. (2006), *Local Approximation Techniques in Signal and Image Processing*, SPIE Press, ISBN 0-8194-6092-3, Bellingham, Washington, USA.

[Kingsbury, 1998] Kingsbury N. G. (1998), "The dual-tree complex wavelet transform: a new efficient tool for image restoration and enhancement". In *Proc. European Signal Processing Conference, EUSIPCO 98*, Rhodes, pp. 319–322, ISBN 960-7620-05-4.

[Kingsbury, 1999] Kingsbury N. G., (1999), "Image processing with complex wavelets". *Philosophical Transactions of the Royal Society London A*, vol. 357 no. 1760, September 1999. pp. 2543–2560, Online ISSN: 1471-2962.

[Kingsbury, 2001] Kingsbury N.G. (2001), "Complex wavelets for shift invariant analysis and filtering of signals", *Journal of Applied and Computational Harmonic Analysis*, 10, no.3 , May, 2001, pp. 234–253, ISSN 1063-5203.

[Kuan et al., 1987] Kuan D. T., Sawchuk A. A. and Strand T. C., (1987), Adaptive restoration of images with speckle, *IEEE Trans. ASSP*, Vol. 35, No. 3, Mars 1987, pp. 373-383, ISSN: 00963518.

[Lee, 1981] Lee J. S., (1981), "Speckle Analysis and Smoothing of Synthetic Aperture Radar Images", *Computer Graphics and Image Processing*, Vol. 17, no.1, September, 1981, pp. 24-32, ISSN: 0146-664X.

[Lurton, 2002] Lurton X., (2002), *An Introduction to Underwater Acoustics*, *Principles and Applications.* Springer, ISBN 3-540-42967-0, Chichester, UK.

[Mallat, 1999] Mallat S. (1999), *A Wavelet Tour of Signal Processing*, Academic Press, ISBN 0-12-466606-X, San Diego, CA, USA.

[Nason, 2002] Nason G. P., (2002), "Choice of wavelet smoothness, primary resolution and threshold in wavelet shrinkage", *Statistics and Computing*, vol. 12, no. 3, Mars, 2002, pp. 219-227, ISSN : 0960-3174.

[Portilla et al., 2003] Portilla J., Strela V., Wainwright M. J. and Simoncelli E. P., (2003), "Image denoising using Gaussian scale mixtures in the wavelet domain," *IEEE Trans. on Image Processing*, vol. 12, no. 11, October 2003, pp. 1338–1351, ISSN: 1057-7149.

[Selesnick, 2001] Selesnick I. W., (2001), "The Characterization and Design of Hilbert Transform Pairs of Wavelet Bases". In *2001 Conference on Information Science and Systems*, The Johns Hopkins University, Mars 21-23, 2001, ISSN 1937-4771.

[Selesnick, 2008] Selesnick I. W., (2008), "The Estimation of Laplace Random Vector in AWGN and the Generalized Incomplete Gamma Function", *IEEE Trans. on Signal Processing*, vol. 56, no. 8, August 2008, pp. 3482-3496, ISSN: 1053-587X .

[Sendur&Selesnick, 2002] Sendur L. and Selesnick I. W., (2002), "Bivariate shrinkage functions for wavelet-based denoising exploiting interscale dependency", *IEEE Trans. on Signal Processing*, vol 50 no. 11, November 2002, pp. 2744-2756, ISSN: 1053-587X.

[Walessa&Datcu, 2000] Walessa M. and Datcu M., (2000), "Model-Based Despeckling and Information Extraction from SAR Images," *IEEE Transactions on Geoscience and Remote Sensing*, vol. 38, no. 5, September 2000, pp. 2258 – 2269, ISSN: 0196-2892.
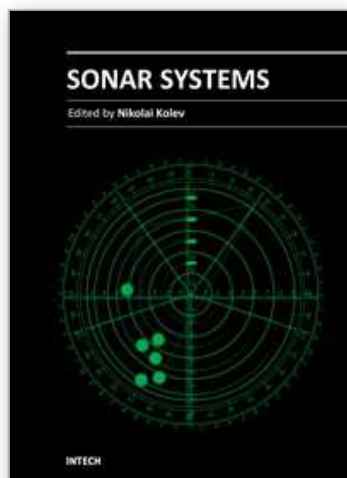
Sonar Systems

Edited by Prof. Nikolai Kolev

The book is an edited collection of research articles covering the current state of sonar systems, the signal processing methods and their applications prepared by experts in the field. The first section is dedicated to the theory and applications of innovative synthetic aperture, interferometric, multistatic sonars and modeling and simulation. Special section in the book is dedicated to sonar signal processing methods covering: passive sonar array beamforming, direction of arrival estimation, signal detection and classification using DEMON and LOFAR principles, adaptive matched field signal processing. The image processing techniques include: image denoising, detection and classification of artificial mine like objects and application of hidden Markov model and artificial neural networks for signal classification. The biology applications include the analysis of biosonar capabilities and underwater sound influence on human hearing. The marine science applications include fish species target strength modeling, identification and discrimination from bottom scattering and pelagic biomass neural network estimation methods. Marine geology has place in the book with geomorphological parameters estimation from side scan sonar images. The book will be interesting not only for specialists in the area but also for readers as a guide in sonar systems principles of operation, signal processing methods and marine applications.

INTECH
open science | open minds